PRE-PRINT doi: 10.1029/2023TC007801

Slowing extrusion tectonics and accelerated uplift of northern Tibet since the mid-Miocene

Haijian Lu[1, 2, 3] *, Xinwen Cao[4], Marco G. Malusà[5], Zhiyong Zhang[6], Jiawei Pan[1, 2, 3], Haibing Li[1, 2, 3]

[1]Key Laboratory of Deep-Earth Dynamics of Ministry of Natural Resources, Institute of Geology, Chinese Academy of Geological Sciences, Beijing 100037

[2]Jiangsu Donghai Crustal Activity in Deep Holes of the Continental Scientific Drilling National Observation and Research Station, Lianyungang 222300

[3]Southern Marine Science and Engineering Guangdong Laboratory (Guangzhou), Guangzhou 511458

[4]Institute of Geomechanics, Chinese Academy of Geological Science, Beijing 100081, China.

[5]University of Milano-Bicocca, Piazza della Scienza 4, 20126 Milano, Italy.

[6]Institute of Geology and Geophysics, Chinese Academy of Sciences, Beijing 100029, China.

Correspondence to: H. Lu, haijianlu2007@126.com

Abstract:

Mechanisms of northern Tibet crustal thickening are strongly debated. Here we present a high-resolution and continuous record (24-4.8 Ma) of anisotropy of magnetic susceptibility and paleomagnetic declination from the Dahonggou section in the northern Qaidam Basin, northern Tibet. Our results reveal two major clockwise rotations of the regional paleostress field at ~15 Ma (~20^{o}) and ~8.4 Ma (~15^{o}), coeval with episodes of mountain building and basin deformation in northern Tibet. We suggest that simultaneous stress field rotation and uplift observed in the study area are related to progressively slowing lateral-extrusion tectonics along boundary-parallel strike-slip faults (Altyn Tagh and Haiyuan faults). The 15 Ma event can be explained by the transition from northeastward to eastward extrusion of northern Tibet materials due to the obstruction of the rigid Alxa block. As deformation

keeps migrating towards the east, the 8 Ma event is possibly related to a change from eastward to southeastward extrusion of northeastern Tibet materials as a result of the resistance of the rigid Ordos block. We conclude that Tibetan deformation evolved through successive stages of slowing extrusion tectonics since the mid-Miocene. Deformation was initially localized along pre-existing lithospheric structures, and subsequently more distributed under confining boundary conditions, leading to crustal thickening and uniform uplift of northern Tibet during the late stage of plateau development.

Plain Language Summary

How northern Tibet evolved as a far-field response to the India-Asian collision remains an open question. Here we present high-resolution and continuous record (24-4.8 Ma) of anisotropy of magnetic susceptibility and paleomagnetic declination from a well-exposed sedimentary section in the northern Qaidam Basin, northern Tibet. The results indicate two significant clockwise rotations (~20^{o} and ~15^{o}) of the regional paleostress field at 15 Ma and 8.4 Ma. Interestingly, these two ages are characterized by large-scale mountain building, basin deformation and initiation or slowdown of major strike-slip faulting in northern Tibet. Given that the relatively weak northern Tibet crust is surrounded by several rigid blocks on its northern and eastern sides, we suggest that Tibetan deformation patterns since the mid-Miocene was associated with successive stages of a weakening extrusion process (from NE- to E-directed extrusion at 15 Ma and from E- to SE-directed extrusion at ~8 Ma) that exploits pre-existing lithospheric weak zones. This study supports the dominant role of strain transfer from localized strike-slip faulting to distributed thickening deformation under confining boundary conditions in raising uniformly the crust of northern Tibet during the late stage of plateau development.

Key points:

1. We present high-resolution anisotropy of magnetic susceptibility and paleomagnetic data from the Neogene sediments in the Qaidam Basin.

2. Our results indicate two major clockwise rotations (~20^{o} and ~15^{o}) of the regional paleostress field at 15 Ma and 8.4 Ma, respectively.

3. We propose a slowing extrusion tectonics and accelerated uplift model to explain the uplift mechanism of northern Tibet in the Neogene.

1 Introduction:

Two end-member models are classically invoked to account for how the vast Tibetan Plateau was formed and is maintained: 1) "Viscous deformation" model assumes that India's northward convergence with Eurasia was mainly accommodated by broadly distributed shortening in the crust and mantle of the Tibetan Plateau (England and Houseman, 1986); 2) "Rigid deformation" model invokes instead displacement and lateral transport of crustal slivers along major strike-slip faults, with tectonic extrusion accommodating most of the convergence between India and Eurasia (Tapponnier et al., 1982). One of the best sites to test these models is northeastern Tibet, which is governed tectonically by a broad areal extent (~500, 000 km^2) of active overthrusting, confined to the south and north by the major Kunlun and Altyn Tagh-Haiyuan fault systems, respectively (Tapponnier et al., 2001). Approximately one-fifth of India's 36-40 mm yr^{-1} northward motion is presently accommodated by compressional and strike-slip structures located in northern Tibet (Zhang et al., 2004; Fig. 1A). Most of the thrust structures appear to be kinematically linked with major strike-slip faults, suggesting a transition from strongly localized deformation along the major faults to distributed deformation near their ends (Burchfiel et al., 1991; Duvall et al. 2010; Kirby et al., 2007; Li et al., 2018; Zhang et al., 2007; Zheng et al., 2013). Current GPS measurements indicate continuous lateral extrusion toward the northeast and southeast in northern Tibet (Fig. 1A; Gan et al., 2007; Zhang et al., 2004). Although there is a growing consensus on the details of present structures of northern Tibet, the main controversy is principally how the crust thickened.

The strike-slip-controlled growth model for northern Tibet (Meyer et al. 1998) is based on the northeastward younging sedimentation onset in the basins south of the

Altyn Tagh fault (ATF) and on the observation that most NW-SE-trending thrust faults branch southeastwards from the ATF and Kunlun fault, which would imply a nearly coeval onset of propagation of strike-slip faulting and crustal thickening (Fig. 2A). The viscous sheet models considering heterogeneous mechanical strength and preexisting weakness in the crust (Kong et al., 1997; Yin et al., 2008) or mantle lithosphere (Clark et al., 2012) were used to explain rapid and efficient stress transfer from the Indo-Asian collision belt to northern Tibet since the Eocene (Fig. 2B). The viscous sheet models also argue for coeval initiation of strike-slip and thrust faulting (Yin et al., 2002). The non-rigid passive bookshelf-fault model claims that continued northeast-trending right-lateral shearing of northern Tibet may drive clockwise rotation of the east-striking left-lateral Kunlun, Qinling, and Haiyuan faults and their surroundings passively against the ATF (Fig. 2C; Zuza and Yin, 2016). This model predicts coeval development of discrete left-lateral faults and distributed off-fault thickening deformation during regional clockwise rotation since the Eocene. Additionally, convective removal of a lithospheric root underlying central Tibet was invoked to account for rapid and uniform uplift of northern Tibet by exerting a high deviatoric compressive stress on the surrounding areas of central Tibet since 20-15 Ma (Fig. 2D; Molnar and Stock, 2009; Yuan et al., 2013; Yue and Liou, 1999). More recently, Zhuang et al. (2018) proposes an external boundary condition model whereby accelerated Pacific-Asia plate convergence was responsible for the onset of rapid topographic growth in northern Tibet beginning at 18-8 Ma. In conclusion, the strike-slip-controlled growth model usually represents “rigid deformation” and the convective removal and external boundary condition models can be classified into “viscous deformation”, whereas the non-rigid passive bookshelf-fault model may be described as a hybrid model between these two end-members.

The sedimentary record preserved in the intermontane basins of northern Tibet can be used to constrain the mechanisms that have caused the rise of the Tibetan Plateau. In this perspective, we performed measurements of anisotropy of magnetic susceptibility (AMS) and paleomagnetic declination at high stratigraphic resolution in the Dahonggou section of the northern Qaidam Basin (Fig. 1B, C), northern Tibet.

The AMS method is a petrofabric tool to determine preferred orientation of particles under an external force, such as gravity, wind, magnetic field, water flow, and strain, during deposition and diagenesis of rocks (e.g., Parés et al., 1999; Li S et al., 2020; Dallanave and Kirscher, 2020). AMS is demonstrated to be efficient in investigating subtle tectonics-related fabrics in weakly deformed or undeformed clay-rich sedimentary sequences undergoing incipient tectonic deformation (Gilder et al., 2001; He et al., 2021; Lu et al., 2014; Li et al., 2020, 2021; Nie et al., 2020; Parés et al., 1999, 2015; Soto et al., 2009; Su et al., 2016; Weil and Yonkee, 2012; Wu et al., 2019; Yu et al., 2014a). The comparison between AMS and paleostress data validates the reliability of AMS ellipsoids as paleostress indicator in compressional settings (e.g., Soto et al., 2009). The exceptionally thick and continuous Dahonggou section is rich in mudrocks that experienced weak deformation by single northeast-directed compressive stress (Yin et al., 2008), making it an ideal location to investigate paleostress field change using AMS data. In addition, magnetostratigraphic data provide the best tool to decipher the distribution, magnitude, and timing of vertical-axis rotations of crustal blocks (Chen et al., 2002; Dupont-Nivet et al., 2002; Li B et al., 2018; Li S et al., 2020; Sun et al., 2005, 2006; Yan et al., 2006; Yu et al., 2014b). Our results reveal two major clockwise rotations of the stress field at 15 and 8.4 Ma, which are combined with existing data sets on the timing of crustal thickening and strike-slip faulting in northern Tibet to propose an improved model and thorough understanding of the dynamic mechanism of crustal thickening of northern Tibet during the late stage of plateau development.

2 Geological setting:

Northern Tibet is characterized by some large, 200- to 600-km-long, parallel (N120^{o}E) ranges with upthrusted basement (the Kunlun, Altyn Tagh, and Qilian Shan) and several high, flat, 30- to 200-km-wide intermontane basins (e.g., Qaidam, Hexi corridor, and Gonghe) (Fig. 1B, 3; Tapponnier et al., 2001). The longest and most continuous lithospheric structures in northern Tibet are the sinistral strike-slip Altyn Tagh, Kunlun, and Haiyuan faults (Fig. 3A). The ATF has a great length of ~1800 km

between 78°E and 97°E and forms a prominent topographic limit between the Tibetan highlands (3000–7000 m a.s.l.) and the Tarim basin (<1000 m a.s.l.). The E–W striking Kunlun fault, extending ~1600 km between 89°E and 105°E, represents the tectonic boundary between the high and flat main Tibet and the relatively low Qaidam Basin. The ~1,000-km-long Haiyuan fault follows the northern edge of the Tibetan Plateau from Hala Lake (~97°E) to Liupan Shan (east of 106°E).

2.1 Crustal rheological heterogeneities between northern Tibet and the surrounding blocks

Northern Tibet is bordered by several rigid blocks, including the Tarim basin to the northwest, the Alxa Block to the north and the Ordos Block to the east (Fig. 1A, 3A). It has steep margins with large variations of crustal thickness and seismic wavespeed (e.g., Tian et al., 2020). The crust thickness is ca. 60 km beneath the Qilian Shan and East Kunlun Shan, but abruptly decrease to 45-50 km under the Tarim and Qaidam basins and the Alxa and Ordos blocks (Tian and Zhang, 2013; Zhao et al., 2013). Although these rigid blocks experienced multiple deformation events during the Paleozoic and Meso-Cenozoic (e.g. Zhang et al., 2022), they are commonly described as a strong resistance to the northward and northeastward growth of Tibet (e.g., Shi et al., 2017; Tian et al., 2020). Therefore, the strong lithospheric heterogeneities along the northern margin of northern Tibet would inhibit outward plateau growth (Chen et al., 2017; Wolf et al., 2022; Xiao et al., 2015).

Detailed seismic imaging of lithospheric structure indicates that the North China craton lithospheric mantle has been underthrust below the Qilian Shan crust (e.g., Ye et al., 2015). Continental subduction induced vertical variations in mechanical properties of the lithosphere, including a thick-skinned crustal accretionary wedges and a middle-lower intracrustal decollement (Ye et al., 2015, 2021; Guo et al., 2016). As large strike-slip faults may be linked at depth with subduction zones, they can accommodate lateral extrusion during continental subduction (Wang et al., 2011). Therefore, the crustal thrust-wedge tectonics above a mid- to lower-intracrustal decollement may accommodate significant tectonic extrusion of the upper crust of

northern Tibet via the strike-slip faulting of the Haiyuan fault (Ye et al., 2015, 2021; Guo et al., 2016).

2.2 Slowing extrusion tectonics along the major faults in northern Tibet

The Cenozoic onset age of left-slip movement along the ATF may vary, depending on the different studies, from early Eocene (~49 Ma; Yin et al., 2002) to latest Oligocene (24±4 Ma; Yue and Liou, 1999; Ritts et al., 2008) and to as late as mid-Miocene (15 Ma; Wu et al., 2012). It is widely accepted that the ATF experienced a two-stage tectonic evolution: large scale (>350 km) and faster (20-30 mm/yr) strike-slip motion from the late Oligocene to the mid-Miocene and slower (<10 mm/yr) strike-slip and distributed shortening and uplift since ~15 Ma, indicating slow extrusion tectonics in northern Tibet after mid-Miocene (Fig. 3A; Li et al., 2021; Yue and Liou, 1999; Ritts et al., 2008; Jian et al., 2018). This hypothesis was later supported by a detailed paleomagnetic study that indicates clockwise and counterclockwise vertical-axis rotations for the Kumkol and Janggalsay basins to the south and north of the ATF, respectively, between the early Miocene and middle Miocene, with no rotation after 15 Ma (Fig. 3A; Lu et al., 2016). Although there are relatively few constraints on the onset timing of strike-slip motion along the Haiyuan fault, some studies indicate consistently that the fault initiated at ~15–10 Ma in the western-central segment (Fig. 3A; Duvall et al., 2013; Li et al., 2019) and at ~8 Ma in the eastern one (Fig. 3A; Zheng et al., 2006; Yuan et al., 2013). The Kunlun fault initiated diachronously at 20–15 Ma along its central segment, at 12-8 Ma in the western segment, and at 8-5 Ma in the eastern one (Fig. 3A; Duvall et al., 2013 and references therein).

Seismic tomography and magnetotelluric survey across the ATF indicate that the fault may reach lithospheric depth of ca. 140 km in its central segment, which decrease dramatically toward its eastern and western tips (e.g., Wittlinger et al., 1998; Xiao et al., 2015). In stark contrast, the Kunlun and Haiyuan faults reach crustal depths of 40-50 km (Wang et al., 2011; Wang et al., 2012; Gao et al., 2013). The ATF is vertical (Wittlinger et al., 1998), whereas the Kunlun and Haiyuan faults dip

209 northward and southward, respectively, and merge with thrust duplex structures in the
210 middle crust (Wang et al., 2011; Gao et al., 2013).
211 Although estimates of the left-lateral offset along the ATF are hotly debated, most
212 authors agree on a cumulative slip exceeding 350 km (Fig. 3A; Chen et al., 2002;
213 Cheng et al., 2015, 2016; Cowgill et al., 2003; Peltzer and Tapponnier, 1988; Yue and
214 Liou, 1999). In comparison, the Kunlun and Haiyuan faults have much lower
215 cumulative offsets not exceeding 100 km (Kidd and Molnar, 1988; Fu and Awata,
216 2007; Gaudemer et al., 1995). Moreover, the Haiyuan Fault show an along-strike
217 variation of left-lateral offset, decreasing from 95±15 km in the central segment to
218 10-15 km at the eastern end (Gaudemer et al., 1995; Burchfiel et al., 1991). This
219 eastward decrease in strike-slip offset, as well as the eastward younging of the
220 initiation timing of strike-slip motion and gradually decreasing depths of these major
221 faults toward their eastern ends, may suggest a slowing extrusion tectonics in
222 northeastern Tibet.
223
224 **2.3 Along-strike variations of slip rates of the major faults in northern Tibet**
225 Numerous studies indicate that late Quaternary strike-slip rates based on
226 geochronology and variously offset geological markers are generally consistent with
227 present-day rates based on global positional system (GPS) and interferometric
228 synthetic aperture radar (InSAR) analyses (Zheng et al., 2013; Zhang et al., 2007;
229 Kirby et al., 2007). The late Quaternary slip rates along the ATF show a nearly
230 identical variation trend from southwest to northeast (Fig. 3B; Table S1). The late
231 Quaternary slip rates along the Kunlun fault remain constant (10-12 mm/yr) in the
232 western-central segment and then decrease from ~10 to ~1 mm/yr from west to east
233 before reaching the eastern plateau margin (Fig. 3C; Table S1). The Quaternary slip
234 rates along the central Haiyuan fault are ~4.5 mm/yr and decrease to ~1 mm/yr along
235 the eastern termination of the fault (Fig. 3D; Table S1). The eastward decreases in
236 strike-slip rate indicate that localized shear strain along the left-lateral strike-slip
237 faults may be replaced by crustal contraction near their eastern terminations (Zheng et
238 al., 2013; Zhang et al., 2007; Kirby et al., 2007; Duvall et al. 2010). Unlike the

Kunlun fault where the strain transfer near its eastern termination is diffusive, the strain transfers end abruptly where the ATF encounters the rigid Alxa Block, and the Haiyuan fault is resisted by the rigid Ordos Block (Li et al., 2018).

2.4 The anisotropy of magnetic susceptibility analyses of the Cenozoic sedimentary rocks in northern Tibet

The AMS fabrics produce kinematic data to be compared to mesostructures such as folds and faults in northern Tibet (Gilder et al., 2001; Lu et al., 2014; Nie et al., 2020; He et al., 2021; Su et al., 2016; Wu et al., 2019; Yu et al., 2014a; Li et al., 2020, 2021). These studies have shown that the orientation of the AMS ellipsoid is in most cases related to the local stress field. Notably, the magnetic lineations (the principal K_{max} axis) observed in the Qaidam Basin show progressive variations with stratigraphic depth (Huo et al., 2020; Li et al., 2020, 2021; Nie et al., 2020; Su et al., 2016; Yu et al., 2014a), likely reflecting temporal changes in tectonic compression direction (Yu et al., 2014a; Li et al., 2020, 2021; Su et al., 2016). However, no further study has been conducted to investigate the variation of tectonic compression direction through time due partly to the debated chronological framework of the Cenozoic strata in the northern Qaidam Basin (Ji et al., 2017; Wang et al., 2017). The relatively clustered magnetic lineation direction is due to the observation that as the deformation evolves to the weak cleavage state, the principal K_{max} axis becomes perpendicular to the shortening direction (e.g., Dallanave and Kirscher, 2020). Until now, two distinct tectonic processes are proposed to account for these changes, i.e., the left-lateral strike-slip motion along the Kunlun fault or the eastward channel flow (Yu et al., 2014a; Su et al., 2016), and the propagation of strike-slip faulting along the ATF into the northern Qaidam marginal thrust belt (Li et al., 2020; Su et al., 2016).

2.5 Differential vertical-axis rotation of crustal blocks within northern Tibet

In strike-slip-dominated northern Tibet, relatively small (generally no more than 40^{o}) rotations of crustal blocks have been inferred from paleomagnetic data of Mesozoic-Cenozoic sedimentary rocks (Fig. 3A; Table S2). By taking the Qinghai

lake and Gonghe extension area as a boundary (Li et al., 2018; Zuza and Yin, 2016), northern Tibet can be divided into two parts: the eastern part experienced clockwise rotations of 10-35^{o}, which are recorded by sedimentary rocks of different ages; whereas the western part shows no wholesale rotation (Fig. 3A; Table S2). The significant rotations of crustal blocks are mainly concentrated along the ATF in the western part of northern Tibet. Although a successive >30^{o} rotation was documented for a relatively long time period of >10 Ma in the Lulehe section (e.g., Li et al., 2018), similar rotations have not been detected in other localities of the Qaidam Basin (Dupont-Nivet et al., 2002; Sun et al., 2005; Yu et al., 2014b; This study). Therefore, such significant rotation may be readily ascribed to a prolonged reactivation of local structural belts in the Lulehe area. In other words, the differential rotation of northern Tibet may be an effect of the different rheology of terranes with different geological histories (Yin and Harrison, 2000).

2.6 Geologic and tectonic setting of the Qaidam Basin and Dahonggou section

The lozenge-shaped Qaidam basin, the biggest intermontane basin in Tibet, is tectonically bounded by the northern Qaidam thrust belt to the north, the sinistral ATF to the west, the Eastern Kunlun thrust belt to the south, and the dextral Wenquan Fault to the east (Fig. 1B), and was controlled by a series of NW- and NWW-trending thrust-fold belts that are roughly perpendicular to the direction of Indo-Asian convergence (Fig. 1A). The basin, covering an area of ~120, 000 km^2, is surrounded by four major mountain ranges: the east Kunlun Shan and Qimen Tagh to the south, the Altyn Tagh Range to the northwest, the Ela Shan to the east, and the Qilian Shan-Nan Shan to the northeast (Fig. 1B, 3). These ranges are ~5000 m in elevation on average, whereas the intervening basin is ~2800 m in elevation and includes widespread and exceptionally thick (>10 km) Mesozoic-Cenozoic terrigenous clastic successions (Cheng et al., 2019; Meng et al., 2001; Wu et al., 2011; Yin et al., 2008; Zhuang et al., 2011; Jian et al., 2019). The Cenozoic deposits are well exposed by NW-trending fold structures within the northern Qaidam basin (Fig. 1C) and reach a thickness of 5-6 km in the Dahonggou and Lulehe sections (QBGMR, 1984). The

axes of folds that deform the Cenozoic Dahonggou deposits generally mimic the strike of the NW-trending Luliang Shan thrusts with the northwest-trending thrust segments linked with the east-northeast-trending lateral ramp segments (Fig. 1C; Yin et al., 2008). As such, the Luliang Shan and Dahonggou strata both exhibit an L-shaped geometry in map view. In summary, the study area was deformed by thrusting and folding under simple NE-directed horizontal compression.

These deposits are classically subdivided into seven formations, including from the bottom to the top the Lulehe, lower Ganchaigou, upper Ganchaigou, lower Youshashan, upper Youshashan, Shizigou, and Qigequan formations (Fig. 4). The lithologies of these seven formations exhibit an initial upward-fining and then upward-coarsening trend (Fig. 4). Magnetostratigraphic studies based on time constraints of fossil ostracode (Ji et al., 2017) and mammal (Wang et al., 2017) yield considerably different basal ages (~52 Ma vs ~25 Ma) for the Cenozoic deposits in the northern Qaidam Basin. Our recent magnetostratigraphic study of the measured ~5300-m-thick Dahonggou section, with a high sampling density (2250 samples), produced a compelling sequence of normal and reverse polarity zones (Fig. S1; Lu et al., 2022). Magnetostratigraphic results in combination with tie points provided by Mid-Miocene mammalian fossils indicate that these deposits span a time interval of ~24-4.8 Ma (Fig. S1; Li and Wang, 2015; Lu et al., 2022).

3 Sampling and methods:

A continuous 5300-m composite section was sampled, consisting of an eastern part (the Lulehe Fm) and a western part (lower Ganchaigou to Shizigou Fm). (Fig. 1C). The samples consist of mudstones and siltstones and minor sandstones with no apparent metamorphic or hydrothermal alteration (Fig. S2). To avoid ambiguous magnetization and potential paleocurrent imprints, no conglomerates and coarse-grained sandstones have been included. The sampling interval was typically 1.5-5 m, reaching ~10 m in the coarsest intervals of the succession. Two specimens were drilled at each sampling level. All samples were oriented with a magnetic compass and then cut into cylindrical specimen (diameter: 2.5 cm, height: 2.2 cm). A

total of 2009 paleomagnetic specimens were used for AMS measurement.

AMS analyses were carried out using an AGICO KLY-4S Kappa Bridge with an automated sample handling system and applied field of 300A/m at a frequency of 875 Hz at Key Laboratory of Paleomagnetism and Tectonic Reconstruction of Ministry of Natural Resource, Chinese Academy of Geological Sciences, Beijing. Each sample was rotated according to three orthogonal planes. All data were processed using the software package of Anisoft 5.0.

The AMS parameters, including $K_{1/2/3}$ (maximum/intermediate/minimum), Km (mean susceptibility), Pj (corrected degree of anisotropy), and T (shape factor) were calculated following the definition of Tarling and Hrouda (1993). Km represents the concentration of paramagnetic and ferromagnetic minerals and was computed as $(K_1+K_2+K_3)/3$; Pj quantifies the degree of anisotropy (Jelinek, 1981); and T reflects the shape of the susceptibility ellipsoid. $0<T\leq1$ indicates oblate shapes, whereas $-1\leq T<0$ represents prolate shapes, and T=0 corresponds to neutral shapes (Jelinek, 1981). The oblate and prolate shapes also correspond to $K_1=K_2>K_3$ and $K_1>K_2=K_3$, respectively. The interval-mean direction of magnetic lineation (the clustering of the K_1 axes) was determined by Fisher mean of declinations of maximum principal axes (Fisher, 1953).

To evaluate the relative contribution of paramagnetic minerals to the total AMS fabric (Parés and van der Pluijm, 2002, 2014; Richter and van der Pluijm, 1994; Schultz-Krutisch and Heller, 1985), we selected 23 representative specimens from the Dahonggou section for low temperature (77K: boiling temperature of liquid nitrogen) AMS (LT-AMS) measurements. The LT-AMS measurement was conducted at the Key Laboratory of Paleomagnetism of the Ministry of Natural Resources, Chinese Academy of Geological Sciences, Beijing according to Issachar et al. (2016).

To determine the percentage of several main minerals, we performed powder X-ray diffraction (XRD) on 54 representative siltstone samples. XRD analyses were conducted using a Dmax 12 kW powder diffractometer (CuKα) at 40 kV and 100 mA, with a sampling width of 0.02^{o} and a scanning speed of 4^{o} (2θ) min^{-1}, at the

MicroStructure Analytical Laboratory of Peking University.

The paleomagnetic declination data of the Dahonggou section were derived from a recently updated magnetostratigraphic study (Lu et al., 2022). We divided 1419 characteristic remanent magnetic directions clustering within 40^{o} of the mean into 14 intervals, each of which has 91–104 specimens. The paleomagnetic declination direction of each interval was calculated using Fisher statistics (Fisher, 1953) on the selected directions.

4 Results:

4.1 XRD data

The siltstone samples are primarily composed of quartz (38-70%), calcite (0-35%), plagioclase (2-30%), microcline (2-14%) and clay minerals (6-23%), and secondarily of hematite (0-1%), gypsum (0-10%), halite (0-8%), and amphibole (0-5%) (Fig. S3; Dataset S1). The Lulehe Fm. samples (E-3, E-47 and E-84) have a relatively high proportion of hematite (1%).

4.2 Anisotropy of magnetic susceptibility data

The magnetic susceptibility of our samples is relatively low, generally in the range 100-500×10^{-6} SI units; the anisotropy degree (Pj) is typically less than 1.15; the shape parameter (T) ranges mostly from -0.75 to 1 (Fig. 5; Dataset S2). In tilt-corrected coordinates, the K_1 directions of all samples are generally subhorizontal and well clustered in an approximately NW-SE direction and are sub-parallel to the strike of bedding plane (Fig. 6) and to the fold axes observed in the Dahonggou section (Fig. 1C). The K_3 axes are near bedding perpendicular and show a slight girdle distribution that is normal to the magnetic lineation direction (Fig. 6). The orientations of these AMS ellipsoids are similar to those from low temperature AMS measurement (Fig. S4). The distribution characteristics of the Dahonggou AMS data are generally consistent with those of previous AMS data in the Qaidam Basin (Huo et al., 2020; Li et al., 2020, 2021; Nie et al., 2020; Su et al., 2016; Yu et al., 2014a).

With the exception of a rapid decrease of Km since ~8 Ma, the AMS parameters

(Km, Pj and T) show no other noticeable change with stratigraphic depth (Fig. 7). To reveal statistically significant variations in magnetic lineation with time, we subdivided the 2009 samples into 20 groups. Each group, except the last, is composed of the same number of samples (~100) (Fig. 8). The samples of the first group are the coarse-grained red bed deposits of the Lulehe Fm. (Fig. S5), which were not taken into further account for the following two reasons: 1) the Lulehe Fm. are coarse-grained conglomeratic and sandy continental red beds. Sedimentological analyses indicate that these sediments were principally deposited in high-energy alluvial fan and braided fluvial environments, thus representing synorogenic deposition (Yin et al., 2008; Zhuang et al., 2011; Lu et al., 2019; Jian et al., 2022). These relatively coarse-grained sandstone samples from the Lulehe Fm. have randomly distributed three principal axes and quite low values of magnetic susceptibility, magnetic foliation and anisotropy degree (Pj) (Fig. 7; Li et al., 2020). Therefore, the AMS results are meaningless for these coarse-grained sandstone samples (Li et al., 2020). 2) The existing magnetostratigraphic studies of the Dahonggou section indicate that relative to the generally consistent results from other formations (Fig. 9; Ji et al., 2017; Lu et al., 2022; Wang et al., 2017), the Lulehe Fm. deposits have distinctly different polarity zone patterns (Fig. 9; Ji et al., 2017; Ke et al., 2013; Lu et al., 2022; Wang et al., 2017). These indeterminate polarity zones suggest that the Lulehe Fm. sediments did not record primary remanent magnetization. Previous studies from southeastern Tibet indicate that these red beds likely have a great quantity of authigenic hematite and goethite with detrital Fe-bearing minerals strongly altered (Huang et al., 2020), which is also consistent with the unusually high percentage of hematite (up to 1%) revealed by XRD analysis (Fig. S3; Dataset S1).

The average directions of magnetic lineation of the other 19 groups can be clearly subdivided into three sets (Fig. 8). The first age interval (22.3-14.9 Ma) ranges from 111.1^{o} to 117^{o}, with a mean of 116.3 ^{o}±5.1 ^{o}; the second one (14.9-8.8 Ma) is comprised between 127 ^{o} and 148.4 ^{o} with an average of 136.5 ^{o}±6.2 ^{o}; and the third one (8.8-4.8 Ma) ranges from 142 ^{o} to 165.5 ^{o}, i.e., 151 ^{o}±33.7 ^{o} on average. In order to obtain more precise time-bounds on the sharp deflections of magnetic lineation

directions through the analyzed section, we further examined high stratigraphic resolution data of AMS K_1 declination (Fig. 7). Two significant time points of 15 Ma and 8.4 Ma were proposed based on the above results (Fig. 7). The corresponding three age intervals now have averages of 115.2 ^{o}, 135.3 ^{o} and 150.5 ^{o} (Fig. 7).

4.3 Paleomagnetic declination data

The declination values of the Dahonggou section vary from -3.4^{o} to 5.2^{o}, showing no significant variation from 24 to 4.8 Ma (Fig. 7 and Table S3). Recently, Li et al. (2018) and Sun et al. (2022) have reported a significant (~24 ^{o}) and successive rotation for the upper Ganchaigou Formation of the Dahonggou section. However, other paleomagnetic studies consistently indicate negligible rotation for the same section (Yu et al., 2014b; Su et al., 2016; Dupont-Nivet et al., 2002).

5 Discussion

5.1 Two pulsed clockwise rotation of stress field at 15 and 8.4 Ma

The low Pj and Km values are controlled by the paramagnetic matrix and specifically the shape anisotropy of clay minerals to the bulk susceptibility (e.g., Rochette, 1987; Hrouda and Kahan, 1991; Tarling and Hrouda, 1993), which is confirmed by low temperature AMS measurement (Fig. S3). XRD analyses also indicate a relatively high proportion of clay minerals (6-23%) in the siltstones of the Dahonggou section (Dataset S1). The distribution characteristics of magnetic fabric of the Dahonggou section suggest that the original sedimentary fabric was overprinted by weak incipient deformation based on the following two lines of evidence: 1) The well-defined magnetic lineations are in sharp contrast to the varied paleocurrent directions throughout the Dahonggou section (Fig. 7); 2). The AMS lineations are mainly subparallel to the orientation of fold axes (Strike: ~135^{o}; Fig. 1C) and the strikes of bedding planes (Fig. 8). According to the conceptual model of AMS development in mudrocks undergoing progressive deformation, the magnetic fabric in sedimentary rocks of the Dahonggou section can be referred to as a "weak cleavage" state (e.g., Parés et al., 1999, 2015; Dallanave and Kirscher, 2020). In summary, the

Dahonggou AMS data record weak tectonic strain during or shortly after sedimentation and subsequent tectonic deformation did not overprint, or even influence the original AMS fabric.

As incipient deformation drives rotation of platy phyllosilicates within the bedding plane, K_1 axes become progressively aligned perpendicular to the shortening direction (Soto, 2009). Therefore, variations in the trend of magnetic lineation are commonly employed to deduce changes of shortening direction in compressive settings. Our AMS results suggest two notable changes in compression direction from N25.2^{o}E to ~N45.3^{o}E at 15 Ma and from N45.3^{o}E to ~N60.5^{o}E at 8.4 Ma (Fig. 6). Sometimes strain and paleostress field reconstruction are complicated by modification of early layer parallel shortening fabrics by later deformation, such as vertical-axis rotations. However, the paleomagnetic declination values of the Dahonggou section indicate no significant variation for the 24-4.8 Ma time span. The finding is consistent with previous paleomagnetic studies of the Dahonggou section (Dupont-Nivet et al., 2002) and other localities (e.g., Sun et al., 2005; Yu et al., 2014b) in the Qaidam Basin, suggesting that the basin did not experience wholesale vertical axis rotation during the Neogene. Such observation was generally attributed to the rigid nature of the Qaidam Basin basement (Zhu et al., 1998). Hence, the two pulsed clockwise rotations of horizontal compression at 15 and 8.4 Ma likely reflect temporal variations in paleostress orientations.

5.2 Regional paleostress field reflected by the Dahonggou AMS data

The Dahonggou section was deposited continuously between ~24 and 4.8 Ma and does not contain growth strata, implying that the Dahonggou strata did not experience local tectonic deformation prior to 4.8 Ma. Subsequently, the Dahonggou section was uplifted and exposed between <4.8 Ma and 2.6 Ma based on magnetostratigraphic dating of the section (Fig. S1) and the stratigraphic contact relationships between the Shizigou and Quaternary Qigequan Fms (Fig. 4H). These observations indicate that the thrust front did not begin to encroach into the Dahonggou locality until ~3 Ma. Interestingly, the fold axis of the Dahonggou section, as well as a series of

NW-trending thrust-fold belts in the Qaidam Basin, is roughly parallel to the Cenozoic Indus–Yalu collisional belt and the northern boundary of the plateau (Fig. 1A). Therefore, the AMS shortening directions recorded in the Dahonggou section likely reflect regional, not local paleostress field. Moreover, in striking contrast to its surroundings with weak crust where various amounts of vertical-axis rotation have been detected (e.g., Chen et al., 2002; Dupont-Nivet et al., 2004; Lu et al., 2016; Yan et al., 2006), the rigid Qaidam Basin did not rotate as a whole after undergoing progressive deformation during the Neogene (Fig. 3A). We thus suggest that the Dahonggou AMS data likely record variations in paleostress orientation affecting northern Tibet.

5.3 Two phases of initiation or acceleration of mountain building and basin deformation in northern Tibet since 15 and 8 Ma

Increasing evidence demonstrates a large-scale simultaneity of compressional deformation across northern Tibet at 15 Ma (Fig. 10A): 1) Substantial tectonic uplift was demonstrated around the ATF by a suite of synorogenic conglomerates with thicknesses >1 km (Lu et al., 2016; Ritts et al., 2008; Sun J et al., 2005; Wang et al., 2016; Zheng et al., 2015), an accelerated exhumation rate of 1.1 km/Ma (Cao et al., 2015), and an almost threefold increase in sediment accumulation rate (Chang et al., 2015). 2) An accelerated uplift of the Qilian Shan was initiated since ~15 Ma (Fang et al., 2007; Li et al., 2019; Wang et al., 2016; Yu et al., 2019; Meng et al., 2020). 3) A nearly E-W shortening deformation began in the Dulan and Jishi Shan since 17-12 Ma and 13 Ma, respectively (Duvall et al., 2013; Lease et al., 2011).

Subsequently, a major propagation of thrust faulting was initiated virtually simultaneously at ~8 Ma (Fig. 10B; Li et al., 2014). The most well-known example is in the NNW-SSE-oriented Liupan Shan where apatite fission track dating of Early Cretaceous sedimentary rocks indicates rapid exhumation around 8 Ma possibly related to E-directed compression (Zheng et al., 2006). A major sediment recycling event at ~8 Ma was identified in three different successions of the northern Qaidam basin based on fission-track analysis of detrital apatite grains (Pang et al., 2019; Lu et

al., 2022), possibly linked to a southward propagation of the deformation front. A similar event is also archived in the Linxia basin, northeastern Tibet (Zheng et al., 2003), and S-directed thrust-related folding is revealed by syn-tectonic growth strata in the Kumkol (Lu et al., 2018), Gonghe (Craddock et al., 2011), and Guide basins (Fang et al., 2005).

In summary, deformation occurring at ~15 Ma was mainly focused along the ATF and related secondary structural belts, whereas deformation at ~8 Ma was widely distributed in northeastern Tibet (Fig. 10). This shift in the locations of these two deformation events may reflect a significant transfer of deformational front in northern Tibet during the Neogene.

5.4 Mechanism of crustal thickening of northern Tibet

Coincidently, the 15 Ma and 8 Ma time frames are also relevant for the activity of the major faults parallel to the margin of the plateau (Altyn Tagh and Haiyuan). Tectono-sedimentary and paleomagnetic vertical-axis rotation studies indicate rapid decreases in the amount and rate of ATF's strike slip since ~15 Ma, when fault deformation was partly converted into widespread crustal shortening in the Qilian, West Kunlun and Altyn ranges (Fig. 3A, 10A; Yue and Liou, 1999; Ritts et al., 2008; Lu et al., 2016; Li et al., 2021). Strike-slip motion along the Haiyuan fault initiated at ~15 Ma along the western/central fault segment and at 10-8 Ma along the eastern fault tip (Fig. 3A, 10A; Duvall et al., 2013; Li et al., 2019).

Existing models of northern Tibet uplift are unable to account for these integrated observations, including two pulsed clockwise rotations of the regional stress field, initiation or deceleration of major strike-slip faulting and two-phase crustal thickening at 15 and 8.4 Ma. Many of the new observations from northern Tibet can be tested against the previous competing models. The strike-slip-controlled growth model requires coeval onset of strike-slip faulting and crustal thickening deformation, which is inconsistent with the two-stage tectonic evolution of the ATF and Kunlun faults. The ATF accommodated fast and localized strike-slip movements from the late Oligocene to the Mid-Miocene, which was replaced by distributed shortening

deformation since ~15 Ma (Li et al., 2021; Lu et al., 2016; Yue and Liou, 1999; Ritts et al., 2008). The Kunlun fault experienced widespread Eocene-Oligocene thrust faulting, which was overprinted by Miocene-Pliocene strike-slip faulting (e.g. Duvall et al., 2013). The viscous sheet model may explain well the early tectonic records broadly coeval with the timing of Indo-Asian collision, but fail to account for the complex Neogene deformational patterns described in northern Tibet. The non-rigid passive bookshelf-fault model explains well the clockwise rotation (10-35^{o}) of the eastern part of northern Tibet, but the wholesale rotation required by this model is not observed in the western part of northern Tibet (Fig. 3A). The convective removal and external boundary condition models did not consider markedly different timings, rates and slip offsets along these three major strike-slip faults in northern Tibet and thus oversimplify the Neogene tectonic evolution of northern Tibet. In particular, the convective removal model is in contrast with some important observations: 1) It is unable to explain the nearly simultaneous onset (~15 Ma) of strike-slip faulting along the Haiyuan and Xianshuihe faults which are roughly orthogonal and parallel, respectively, to the maximum principal stress stemmed from the detached lithospheric mantle under central Tibet; 2) It cannot account for multiple episodes (e.g. ca. 15 Ma and 8 Ma) of rapid uplift of northern Tibet which would require repeated removal of central Tibet mantle lithosphere within a relatively short time interval; 3) This model predicts NNE-SSW contraction for northern Tibet and therefore fails to explain the E-W-oriented compressional deformations observed in the Dulan and Jishi Shan since 17-12 Ma and 13 Ma, respectively (Duvall et al., 2013; Lease et al., 2011).

Therefore, we develop a continuous geodynamic scenario to explain the observations above, featuring nearly simultaneous initiation, or deceleration of strike-slip movement, crustal thickening and stress field rotation. First, the change in tectonic deformation along the ATF and adjacent Qilian and West Kunlun Shan at 15 Ma may be related to the northeastward tectonic extrusion of northern Tibet crust along the ATF, which was obstructed by the rigid Alxa Block (Fig. 10A). The oblique northeastward movement of northern Tibet toward the rigid Alxa Block led to strain partitioning at the eastern tip of the ATF, triggering not only one of the most important

uplift episodes of northern Tibet since ~15 Ma, but also leading to the dissipation and the initiation of fast strike-slip motion along the ATF and Haiyuan fault, respectively, at this time. The synchronous onset of strike-slip motion along the Haiyuan fault and a significant clockwise rotation (~20^{o}) of paleostress field imply that northern Tibet rocks began to be extruded eastward since ~15 Ma. This is demonstrated in the Changma Basin, northwestern corner of northern Qilian Shan, where paleomagnetic and structural evidence indicate a significant clockwise rotation of the basin and the presence of several roughly north-south-trending arcuate extensional faults, respectively (Li et al., 2006). Subsequently, the eastward extrusion of northern Tibet rocks along the Haiyuan fault was blocked by the rigid Ordos Block at ~8 Ma. Strain partitioning in the transpressional zone near the eastern end of the Haiyuan fault may explain the dissipation of strike-slip motion of the Haiyuan fault toward the east, abrupt uplift of the Liupan Shan and its surroundings and clockwise rotation of the crust south of the fault (Zheng et al., 2013; Li et al., 2018). This clockwise rotation suggests that some northeastern Tibet materials began to move from eastward to southeastward. This transition favored not only tectonic encroachment into the southwestern corner of the Ordos Block and the western end of the Weihe Graben (Zhang et al., 1995), but also the ~15^{o} clockwise rotation of the stress field and the southward propagation of deformation front into the intermontane basins of northern Tibet (Fig. 10B). The kinematic shift from eastward to southeastward tectonic extrusion gains support from deep seismic reflection data, which indicate the existence of a laterally continuous crustal wedge (Guo et al., 2016). The conveyor belt-like crustal wedge configuration that assists oblique sinistral motion transported crustal materials eastward toward the Ordos Block between 15 and 8 Ma and then southeastward toward the Qinling orogen after 8 Ma (Guo et al., 2016).

We propose that the progressive confinement of the relatively weak Tibet crust against the rigid crustal blocks to the northeast and then to the east led to uniform crustal thickening of northern Tibet (Fig. 11). This interpretation highlights the major role of boundary conditions in determining whether a deforming zone is laterally confined during the late stage of plateau development. In our model, lateral motion

along the faults parallel to the range was precluded by the surrounding Alxa and Ordos cratons with consequent strain partitioning in zones of oblique convergence (Fig. 11). The major strike-slip faults acted as transfer-fault structures linking dip-slip fault systems at their eastern ends (Burchfiel et al., 1991; Duvall and Clark, 2010). The smaller faults between the Kunlun and Haiyuan strike-slip faults, such as the southeast-striking right-lateral Elashan and Riyueshan faults, contributed in accommodating eastward lateral extrusion of northern Tibet materials (Duvall and Clark, 2010; Zuza and Yin, 2016).

5.5 Implications for the tectonic evolution of northern Tibet

Our model of progressively weakening lateral extrusion indicates a transfer of most of fast left-lateral slip along the ATF eastward to the left-lateral Haiyuan and Kunlun faults and to distributed deformation across a wider deforming zone between the two faults and to local clockwise rotation of some subordinate crustal blocks (e.g., the Changma basin). This study highlights the significance of the ATF in controlling the Neogene tectonic evolution of northern Tibet (Fig. 11). The ATF has a much larger slip offset and shear depth and more prolonged movement history than the Haiyuan and Kunlun faults. However, these significant differences and the potential kinematic shift between these major faults were not taken into account by some previous studies (e.g., Yuan et al., 2013).

In addition, given cumulative offset of >350 km along the ATF and ≤100 km along the Haiyuan and Kunlun faults, our model acknowledges the importance of strike-slip faulting in accommodating the Indo-Asian collision (Tapponnier et al., 1982), especially during the early stage of fault development with relatively “free” boundaries. In the unilaterally confined experiments, the major faults allow displacement toward the free side with a much larger offset than those in the bilaterally confined experiments (Tapponnier et al., 1982). Later on, the eastward-extruding motion of crustal blocks toward a lateral confining boundary raises the plateau uniformly, supporting the existence of viscous deformation

(England and Houseman, 1986). Although the exact quantitative partitioning of the deformation between shortening and extrusion remains unresolved, the viscous and rigid deformation models likely play equally important roles in absorbing India's northward convergence with Eurasia at different stages.

6 Conclusion:

Our integrated analyses of AMS and paleomagnetic declination from the Dahonggou section in northern Qaidam basin (northern Tibet) identifies two significant clockwise rotations (~20^{o} and ~15 ^{o}) of paleostress field at 15 Ma and 8.4 Ma for northern Tibet. Combined with nearly simultaneous initiation or deceleration of major strike-slip faulting and tectonic uplift at 15 Ma and 8 Ma, a successively decreased lateral extrusion scenario along two boundary-parallel strike-slip faults (Altyn Tagh and Haiyuan) under restricted boundary conditions is proposed to explain the mechanism of coeval crustal thickening of northern Tibet during the late stage of plateau development.

Acknowledgments.

This work was funded by the Second Tibetan Plateau Scientific Expedition and Research Program (2019QZKK0901) and the China Geological Survey (DD20221630). We appreciate the valuable discussions with Zhiming Sun, Shihu Li, and Yong Cao, and the constructive reviews by three anonymous reviewers and associate editor.

Data Availability Statement

Supplementary data supporting the conclusions is available on the research data repository of the Dryad (https://doi.org/10.5061/dryad.mcvdnck49).

Figure captions:

Fig. 1. Geological setting of the Tibetan Plateau and study area. A: Color-shaded relief map of the

Tibetan Plateau and its surroundings with Global positioning system velocities relative to stable Eurasia (Zhang et al., 2004). Bold white arrows indicate N20^{o}E shortening across the plateau interior. Rounded rectangles show the amount of accommodation of India's 36-40 mmyr^{-1} northward motion within different terranes. B: Tectonic setting of the Qaidam Basin and its surroundings. C: Geological map of the Dahonggou section.

Fig. 2. Four main models proposed to explain the crustal thickening mechanism of north Tibet. See text for details.

Fig. 3. Onset ages (A), total offsets (A), and along-strike variation of slip rate (B-D) of the major Altyn Tagh, Kunlun, and Haiyuan faults. Please refer to the section of geological setting and to Table. S1 for details on the onset ages and total offsets of these three major faults and the distribution of strike-slip rates along these three major faults, respectively. Fig. 3A also show vertical-axis rotation data of the Mesozoic-Cenozoic strata in northern Tibet (See Table S2 for details). The inset map in Fig. 3A shows a two-stage evolution model for the ATF, adapted from Ritts et al. (2008).

Fig. 4. Cross section and photographs of the Dahonggou section. A: Google earth image of the well-exposed Dahonggou section; B: Schematic cross section of the Dahonggou strata; C-H: Representative lithofacies of six sedimentary formations.

Fig. 5. Anisotropy of magnetic susceptibility (AMS) results from the Dahonggou section, including the frequency of bulk magnetic susceptibility, Pj-Km, T-Km, and T-Pj diagrams.

Fig. 6. Equal-area projections of the maximum (K_1, blue dots) and minimum (K_3, green triangles) principle axes of AMS divided into different age intervals as explained in the main text. A: Left hand diagram: equal-area projections of the K_1 and K_3 axes of all samples in geographic coordinate; Right hand diagram: the mean magnetic lineation directions of three age intervals (lines with arrows) and the corresponding AMS shortening directions (dashed lines with arrows); B: Equal-area projections of the K_1 and K_3 axes of various age intervals in tilt-corrected coordinate. Red stars indicate the mean K_1 values. Orange arrows denote compression direction.

Fig. 7. Lithology, paleocurrent direction (Bush et al., 2016), mean susceptibility (Km), corrected degree of anisotropy (Pj), shape parameter (T), sedimentary rate, paleomagnetic declination, and declinations of maximum principle axes (K_1_Dec) versus depth from the Dahonggou section. The red bed deposits of the Lulehe Fm. are marked in brick red. Red arrows indicate mean values of

paleocurrent data (n is the number of measured data). The orange lines show the mean K_1_Dec values of three age intervals and the blue curved line indicates 7-point average. The data of sedimentary rate and paleomagnetic declination are calculated from Lu et al. (2022). Refer to Fig. 5 and Fig. S1 for the representative photos and detailed magnetic polarity stratigraphy and correlation with the geomagnetic polarity time scale (GPTS: Hilgen et al., 2012) of this section, respectively.

Fig. 8. Equal-area projections of the tilt-corrected maximum (K_1, blue dots) and minimum (K_3, green triangles) principle axes of the AMS divided into 20 age intervals. Each group, except the last one, has 100-102 samples. Red stars and lines represent the mean values of the K_1 axes and bedding attitudes, respectively. Lines in the central bigger circle show the directions of magnetic lineation of groups 2-20; Lines with arrows indicate the mean directions of magnetic lineation of three consecutive age intervals (22.3-14.9, 14.9-8.8, and 8.8-4.8 Ma).

Fig. 9. The existing magnetostratigraphic studies (Ji et al., 2017; Ke et al., 2013; Lu et al., 2022; Wang et al., 2017) from the Dahonggou locality which show distinctly different polarity zones for the Lulehe red bed deposits (marked in light yellow). For ease of comparison, the time interval of Ji et al. (2017) was reinterpreted based on our preferred magnetic polarity correlation to the GPTS (Hilgen et al., 2012).

Fig. 10. Slowing tectonic extrusion model under restricted boundary conditions used to explain the mechanism of crustal thickening of northern Tibet. A: Summary of tectonic events occurring at Aertashi (Zheng et al., 2015), Kekeya (Zheng et al., 2015), Sanju (Cao et al., 2015), Janggalsay (Lu et al., 2014), Kumukol (Lu et al., 2016), Huatugou (Chang et al., 2015), Miran (Ritts et al., 2008), Tiejianggou (Sun J et al., 2005), and Caogou (Wang et al., 2016) along the ATF and at Qaidam Shan (Meng et al., 2020), Huaitoutala (Fang et al., 2007), Qilian (Yu et al., 2019), Dulan (Duvall et al., 2013), Menyuan (Li et al., 2019), and Jishi Shan (Lease et al., 2011) in northern Tibet at ~15 Ma. Red arrows denote relative motion with respect to the adjacent rigid blocks. Black and red lines indicate inactive and active deformation, respectively; B: Summary of tectonic events occurring at Liupan Shan (Zheng et al., 2006), Linxia (Zheng et al., 2003), Guide (Fang et al., 2005), Gonghe (Craddock et al., 2011), Huaitoutala (Pang et al., 2019), Lulehe (Lu et al., 2022), Dahonggou (Lu et al., 2022), and Kumukol (Lu et al., 2018) in northern Tibet at ~8 Ma.

Fig. 11. Block diagrams illustrating significant strain transfer from localized strike-slip faulting to

distributed thickening deformation under confining boundary condition. Blue symbols indicate newly initiated motion of crustal blocks or deformation.

References:

Burchfiel, B., Zhang, P., Wang, Y., Zhang, W., Song, F., Deng, Q., Molnar, P., Royden, L., 1991. Geology of the Haiyuan fault zone, Ningxia-Hui autonomous region, China, and its relation to the evolution of the northeastern margin of the Tibetan plateau. Tectonics 10, 1091-1110.

Cao, K., Wang, G. C., Bernet, M., van der Beek, P., Zhang, K. X., 2015. Exhumation history of the West Kunlun Mountains, northwestern Tibet: Evidence for a long-lived, rejuvenated orogen. Earth and Planetary Science Letters 432, 391-403.

Chang, H., Li, L., Qiang, X., Garzione, C.N., Pullen, A., An, Z., 2015. Magnetostratigraphy of Cenozoic deposits in the western Qaidam Basin and its implication for the surface uplift of the northeastern margin of the Tibetan Plateau. Earth & Planetary Science Letters 430, 271-283.

Chen, J., Burbank, D., Scharer, K., Sobel, E., Yin, J., Rubin, C., Zhao, R.J.E., Letters, P.S., 2002. Magnetochronology of the Upper Cenozoic strata in the Southwestern Chinese Tian Shan: rates of Pleistocene folding and thrusting. Earth and Planetary Science Letters 195, 113-130.

Chen, L., Capitanio, A.F., Liu, L., Gerya, V.T., 2017. Crustal rheology controls on the Tibetan Plateau formation during India-Asia convergence. Nature Communications 8, 15992.

Cheng, F., Jolivet, M., Dupont-Nivet, G., Wang, L., Yu, X., Guo, Z., 2015. Lateral extrusion along the Altyn Tagh Fault, Qilian Shan (NE Tibet): insight from a 3D crustal budget. Terra Nova 27, 416-425.

Cheng, F., Jolivet, M., Fu, S., Zhang, C., Zhang, Q., Guo, Z., 2016. Large-scale displacement along the Altyn Tagh Fault (North Tibet) since its Eocene initiation: Insight from detrital zircon U–Pb geochronology and subsurface data. Tectonophysics 677-678, 261-279.

Cheng, F., Jolivet, M., Guo, Z., Lu, H., Zhang, B., Li, X., Zhang, D., Zhang, C., Zhang, H., Wang, L., 2019. Jurassic–Early Cenozoic Tectonic Inversion in the Qilian Shan and Qaidam Basin, North Tibet: New Insight From Seismic Reflection, Isopach Mapping, and Drill Core Data. Journal of Geophysical Research: Solid Earth 124, 12077-12098.

Clark, M.K., 2012. Continental collision slowing due to viscous mantle lithosphere rather than topography. Nature 483, 74-77.

Cowgill, E., Yin, A., Harrison, T.M., Wang, X., 2003. Reconstruction of the Altyn Tagh fault based on U-Pb geochronology: Role of back thrusts, mantle sutures, and heterogeneous crustal strength in forming the Tibetan Plateau. Journal of Geophysical Research Solid Earth 108, 457-470.

Craddock, W., Kirby, E., Zhang, H., 2011. Late Miocene–Pliocene range growth in the interior of the northeastern Tibetan Plateau. Lithosphere 3, 420-438.

Dallanave, E., and U. Kirscher (2020), Testing the reliability of sedimentary paleomagnetic datasets for paleogeographic reconstructions, Frontiers in Earth Science, 8, 592277.

Dupont-Nivet, G., Butler, R.F., Yin, A., Chen, X., 2002. Paleomagnetism indicates no Neogene rotation of the Qaidam Basin in northern Tibet during Indo-Asian collision. Geology 30, 263-266.

Dupont-Nivet, G., Horton, B., Butler, R.F., Wang, J., Zhou, J., Waanders, G., 2004. Paleogene clockwise tectonic rotation of the Xining-Lanzhou region, northeastern Tibetan Plateau. Journal of Geophysical Research: Solid Earth 109, B04401.

Duvall, A.R., Clark, M.K., 2010. Dissipation of fast strike-slip faulting within and beyond northeastern Tibet.

Geology 38, 223-226.
Duvall, A.R., Clark, M.K., Kirby, E., Farley, K.A., Craddock, W.H., Li, C., Yuan, D.Y., 2013. Low-temperature thermochronometry along the Kunlun and Haiyuan Faults, NE Tibetan Plateau: Evidence for kinematic change during late-stage orogenesis. Tectonics 32, 1190-1211.
England, P., Houseman, G., 1986. Finite strain calculations of continental deformation: 2. Comparison with the India-Asia collision zone. Journal of Geophysical Research: Solid Earth 91, 3664-3676.
Fang, X., Yan, M., Van der Voo, R., Rea, D.K., Song, C., Parés, J.M., Gao, J., Nie, J., Dai, S., 2005. Late Cenozoic deformation and uplift of the NE Tibetan Plateau: Evidence from high-resolution magnetostratigraphy of the Guide Basin, Qinghai Province, China. GSA Bulletin 117, 1208-1225.
Fang, X., Zhang, W., Meng, Q., Gao, J., Wang, X., King, J., Song, C., Dai, S., Miao, Y., 2007. High-resolution magnetostratigraphy of the Neogene Huaitoutala section in the eastern Qaidam Basin on the NE Tibetan Plateau, Qinghai Province, China and its implication on tectonic uplift of the NE Tibetan Plateau. Earth and Planetary Science Letters 258, 293-306.
Fisher, R., 1953. Dispersion on a sphere. Proceedings of the Royal Society of London. Series A. Mathematical and Physical Sciences 217, 295-305.
Fu, B., Awata, Y., 2007. Displacement and timing of left-lateral faulting in the Kunlun Fault Zone, northern Tibet, inferred from geologic and geomorphic features. Journal of Asian Earth Sciences 29, 253-265.
Gan, W., Zhang, P., Shen, Z.K., Niu, Z., Wang, M., Wan, Y., Zhou, D., Cheng, J., 2007. Present-day crustal motion within the Tibetan Plateau inferred from GPS measurements. Journal of Geophysical Research: Solid Earth 112.
Gao, R., Wang, H., Yin, A., Dong, S., Kuang, Z., Zuza, A.V., Li, W., Xiong, X., 2013. Tectonic development of the northeastern Tibetan Plateau as constrained by high-resolution deep seismic-reflection data. Lithosphere 5, 555-574.
Gaudemer, Y., Tapponnier, P., Meyer, B., Peltzer, G., Shunmin, G., Zhitai, C., Huagung, D., Cifuentes, I., 1995. Partitioning of crustal slip between linked, active faults in the eastern Qilian Shan, and evidence for a major seismic gap, the 'Tianzhu gap', on the western Haiyuan Fault, Gansu (China). Geophysical Journal International 120, 599-645.
Gilder, S., Chen, Y., Sen, S., 2001. Oligo-Miocene magnetostratigraphy and rock magnetism of the Xishuigou section, Subei (Gansu Province, western China) and implications for shallow inclinations in central Asia. Journal of Geophysical Research: Solid Earth 106, 30505-30521.
Guo, X., Gao, R., Li, S., Xu, X., Huang, X., Wang, H., Li, W., Zhao, S., Li, X., 2016. Lithospheric architecture and deformation of NE Tibet: New insights on the interplay of regional tectonic processes. Earth Planetary Science Letters 449, 89-95.
He, C., Zhang, Y., Li, S., Wang, K., Ji, J., 2021. Magnetostratigraphic study of a Late Cretaceous-Paleogene succession in the eastern Xining basin, NE Tibet: Constraint on the timing of major tectonic events in response to the India-Eurasia collision. GSA Bulletin 133, 2457-2484.
Hilgen, F. J., Lourens, L. J., Van Dam, J. A., 2012. In F. M. Gradstein, et al. (Eds.), The Neogene period in Geologic time scale 2012. Elsevier 229, 923–978.
Hrouda, F., 1991. The magnetic fabric relationship between sedimentary and basement nappes in the High Tatra Mountains, N. Slovakia. Journal of Structural Geology 13, 431-442.
Huang, W., Jackson, M.J., Dekkers, M.J., Solheid, P., Zhang, Y., Li, S., Guo, Z., Ding, L., 2020. Remagnetization of red beds on the Tibetan Plateau: Mechanism and diagnosis. Journal of Geophysical Research: Solid Earth 125, e2020JB020068.
Huo, F., Shao, R., Jiang, N., Zhang, R., Cheng, X., Zhang, W., Wei, B., Zhou, Y., Wu, H., 2020. Anisotropy of magnetic susceptibility of Mesozoic and Cenozoic sediments in the northern margin of Qaidam Basin and its

sedimentary-tectonic significance. Chinese Journal of Geophysics 63, 583-596.
Issachar, R., Levi, T., Lyakhovsky, V., Marco, S., Weinberger, R., 2016. Improving the method of low-temperature anisotropy of magnetic susceptibility (LT-AMS) measurements in air. Geochemistry, Geophysics, Geosystems 17, 2940-2950.
Jelinek, V. (1981), Characterization of the magnetic fabric of rocks, Tectonophysics, 79(3-4), T63-T67.
Ji, J., Zhang, K., Clift, P., Zhuang, G., Song, B., Ke, X., Xu, Y., 2017. High-resolution magnetostratigraphic study of the Paleogene-Neogene strata in the Northern Qaidam Basin: Implications for the growth of the Northeastern Tibetan Plateau. Gondwana Research 46, 141-155.
Jian, X., W. Zhang, H. Liang, P. Guan, and L. Fu (2019), Mineralogy, petrography and geochemistry of an early Eocene weathering profile on basement granodiorite of Qaidam basin, northern Tibet: Tectonic and paleoclimatic implications, Catena, 172, 54-64.
Jian, X., P. Guan, W. Zhang, H. Liang, F. Feng, and L. Fu (2018), Late Cretaceous to early Eocene deformation in the northern Tibetan Plateau: Detrital apatite fission track evidence from northern Qaidam basin, Gondwana Research, 60, 94-104.
Jian, X., L. Fu, P. Wang, P. Guan, W. Zhang, H. Fu, and H. Mei (2022), Sediment provenance of the Lulehe Formation in the Qaidam basin: Insight to initial Cenozoic deposition and deformation in northern Tibetan plateau, Basin Research, https://doi.org/10.1111/bre.12712.
Ke, X., Ji, J., Zhang, K., Kou, X., Song, B., Wang, C., 2013. Magnetostratigraphy and anisotropy of magnetic susceptibility of the Lulehe Formation in the northeastern Qaidam Basin. Acta Geologica Sinica-English Edition 87, 576-587.
Kidd, W.S., Molnar, P., 1988. Quaternary and active faulting observed on the 1985 Academia Sinica-Royal Society Geotraverse of Tibet. Philosophical Transactions of the Royal Society of London. Series A, Mathematical Physical Sciences 327, 337-363.
Kirby, E., Harkins, N., Wang, E., Shi, X., Fan, C., Burbank, D., 2007. Slip rate gradients along the eastern Kunlun fault. Tectonics 26, TC2010.
Lease, R.O., Burbank, D.W., Clark, M.K., Farley, K.A., Zheng, D., Zhang, H., 2011. Middle Miocene reorganization of deformation along the northeastern Tibetan Plateau. Geology 39, 359-362.
Li, B., Chen, X., Zuza, A.V., Hu, D., Ding, W., Huang, P., Xu, S., 2019. Cenozoic cooling history of the North Qilian Shan, northern Tibetan Plateau, and the initiation of the Haiyuan fault: Constraints from apatite-and zircon-fission track thermochronology. Tectonophysics 751, 109-124.
Li, B., Yan, M., Zhang, W., Fang, X., Yang, Y., Zhang, D., Chen, Y., Guan, C., 2018. Paleomagnetic rotation constraints on the deformation of the northern Qaidam marginal thrust belt and implications for strike-slip faulting along the Altyn Tagh Fault. Journal of Geophysical Research: Solid Earth 123, 7207-7224.
Li, B., Yan, M., Zhang, W., Fang, X., Yang, Y., Zhang, D., Guan, C., Bao, J., 2021. Two-stage strike-slip faulting of the Altyn Tagh Fault revealed by magnetic fabrics in the Qaidam Basin. Tectonophysics 821, 229142.
Li, B., Yan, M., Zhang, W., Parés, J.M., Fang, X., Yang, Y., Zhang, D., Guan, C., Bao, J., 2020. Magnetic fabric constraints on the cenozoic compressional strain changes in the Northern Qaidam marginal thrust belt and their tectonic implications. Tectonics 39, e2019TC005989.
Li, H., Yang, J., Xu, Z., Sun, Z., Tapponnier, P., Van Der Woerd, J., Meriaux, A., 2006. The constraint of the Altyn Tagh fault system to the growth and rise of the northern Tibetan plateau. Earth Science Frontiers 13(4), 59-79.
Li, J., Fang, X., Song, C., Pan, B., Ma, Y., Yan, M., 2014. Late Miocene–Quaternary rapid stepwise uplift of the NE Tibetan Plateau and its effects on climatic and environmental changes. Quaternary Research 81, 400-423.
Li, S., D. J. van Hinsbergen, Z. Shen, Y. Najman, C. Deng, and R. J. G. R. L. Zhu (2020), Anisotropy of magnetic susceptibility (AMS) analysis of the Gonjo Basin as an independent constraint to date Tibetan shortening pulses,

47(8), e2020GL087531.
Li, Y., Liu, M., Wang, Q., Cui, D., 2018. Present-day crustal deformation and strain transfer in northeastern Tibetan Plateau. Earth Planetary Science Letters 487, 179-189.
Lu, H., Cao, X., Malusa, M. (2023). AMS and XRD data [Dataset]. Dryad. https://doi.org/10.5061/dryad.mcvdnck49.
Lu, H., Fu, B., Shi, P., Ma, Y., Li, H., 2016. Constraints on the uplift mechanism of northern Tibet. Earth and Planetary Science Letters 453, 108-118.
Lu, H., Fu, B., Shi, P., Xue, G., Li, H., 2018. Late-Miocene thrust fault-related folding in the northern Tibetan Plateau: Insight from paleomagnetic and structural analyses of the Kumkol basin. Journal of Asian Earth Sciences 156, 246-255.
Lu, H., Malusà., M.G., Zhang., Z., Guo, L., Shi, X., Ye, J., Sang, S., 2022. Syntectonic sediment recycling controls eolian deposition in eastern Asia. Geophysical Research Letter, 49, e2021GL096789.
Lu, H., Wang, E., Meng, K., 2014. Paleomagnetism and anisotropy of magnetic susceptibility of the Tertiary Janggalsay section (southeast Tarim basin): Implications for Miocene tectonic evolution of the Altyn Tagh Range. Tectonophysics 618, 67-78.
Meng, Q., Song, C., Nie, J., Liu, C., He, P., Liu, F., Li, L., 2020. Middle-late Miocene rapid exhumation of the southern Qilian Shan and implications for propagation of the Tibetan Plateau. Tectonophysics 774, 228279.
Meng, Q.R., Hu, J.M., Yang, F.Z., 2001. Timing and magnitude of displacement on the Altyn Tagh fault: constraints from stratigraphic correlation of adjoining Tarim and Qaidam basins, NW China. Terra Nova 13, 86-91.
Meyer, B., Tapponnier, P., Bourjot, L., Metivier, F., Gaudemer, Y., Peltzer, G., Shunmin, G., Zhitai, C., 1998. Crustal thickening in Gansu-Qinghai, lithospheric mantle subduction, and oblique, strike-slip controlled growth of the Tibet plateau. Geophysical Journal International 135, 1-47.
Molnar, P., Stock, J.M., 2009. Slowing of India's convergence with Eurasia since 20 Ma and its implications for Tibetan mantle dynamics. Tectonics 28, TC3001.
Nie, J., Ren, X., Saylor, J.E., Su, Q., Pfaff, K., 2020. Magnetic polarity stratigraphy, provenance, and paleoclimate analysis of Cenozoic strata in the Qaidam Basin, NE Tibetan Plateau. Geological Society of America Bulletin 132, 310-320.
Pang, J., Yu, J., Zheng, D., Wang, W., Ma, Y., Wang, Y., Li, C., Li, Y., Wang, Y., 2019. Neogene expansion of the Qilian Shan, north Tibet: Implications for the dynamic evolution of the Tibetan Plateau. Tectonics 38, 1018-1032.
Parés, J.M., 2015. Sixty years of anisotropy of magnetic susceptibility in deformed sedimentary rocks. Frontiers in Earth Science 3, 4.
Parés, J.M., van der Pluijm, B.A., 2002. Phyllosilicate fabric characterization by low-temperature anisotropy of magnetic susceptibility (LT-AMS). Geophysical Research Letters 29, 68-61-68-64.
Parés, J.M., van der Pluijm, B.A., 2014. Low-temperature AMS and the quantification of subfabrics in deformed rocks. Tectonophysics 629, 55-62.
Parés, J.M., van der Pluijm, B.A., Dinarès-Turell, J., 1999. Evolution of magnetic fabrics during incipient deformation of mudrocks (Pyrenees, northern Spain). Tectonophysics 307, 1-14.
Peltzer, G., Tapponnier, P., 1988. Formation and evolution of strike-slip faults, rifts, and basins during the India-Asia collision: An experimental approach. Journal of Geophysical Research: Solid Earth 93, 15085-15117.
QBGMR, 1984. Geologicmap of the Daqaidam Sheet. Beijing Geological Publishing House, scale 1: 200,000.
Richter, C., van der Pluijm, B.A., 1994. Separation of paramagnetic and ferrimagnetic susceptibilities using low temperature magnetic susceptibilities and comparison with high field methods. Physics of the Earth Planetary

Interiors 82, 113-123.
Ritts, B.D., Yue, Y., Graham, S.A., Sobel, E.R., Abbink, O.A., Stockli, D., 2008. From sea level to high elevation in 15 million years:Uplift history of the northern Tibetan Plateau margin in the Altun Shan. American Journal of Science 308, 657-678.
Rochette, P., 1987. Magnetic susceptibility of the rock matrix related to magnetic fabric studies. Journal of Structural Geology 9, 1015-1020.
Schultz-Krutisch, T., Heller, F., 1985. Measurement of magnetic susceptibility anisotropy in Buntsandstein deposits from southern Germany. Journal of Geophysics 57, 51-58.
Shi, J., Shi, D., Shen, Y., Zhao, W., Xue, G., Su, H., Song, Y., 2017. Growth of the northeastern margin of the Tibetan Plateau by squeezing up of the crust at the boundaries. Scientific reports 7, 1-7.
Soto, R., Larrasoaña, J.C., Arlegui, L.E., Beamud, E., Oliva-Urcia, B., Simón, J.L., 2009. Reliability of magnetic fabric of weakly deformed mudrocks as a palaeostress indicator in compressive settings. Journal of Structural Geology 31, 512-522.
Su, Q., Nie, J., Saylor, J.E., Horton, B.K., Bush, M., Chen, W., 2016. An anisotropy of magnetic susceptibility study of the Cenozoic Dahonggou section in northern Qaidam Basin and its tectonic implications. Quaternary Sciences 36, 859-869.
Sun, J., Zhu, R., An, Z., 2005. Tectonic uplift in the northern Tibetan Plateau since 13.7 Ma ago inferred from molasse deposits along the Altyn Tagh Fault. Earth and Planetary Science Letters 235, 641-653.
Sun, Z., Yang, Z., Pei, J., Ge, X., Wang, X., Yang, T., Li, W., Yuan, S., 2005. Magnetostratigraphy of Paleogene sediments from northern Qaidam Basin, China: implications for tectonic uplift and block rotation in northern Tibetan plateau. Earth Planetary Science Letters 237, 635-646.
Sun, Z., Yang, Z., Pei, J., Yang, T., Wang, X., 2006. New Early Cretaceous paleomagnetic data from volcanic and red beds of the eastern Qaidam Block and its implications for tectonics of Central Asia. Earth Planetary Science Letters 243, 268-281.
Tapponnier, P., Peltzer, G., Le Dain, Y.A., Armijo, R., Cobbold, P., 1982. Propagating extrusion tectonics in Asia: New insights from simple experiments with plasticine GEOLOGY 10, 611-616.
Tapponnier, P., Xu, Z., Françoise, R., Bertrand, M., Nicolas, A., Gérard, W., Yang, J., 2001. Oblique stepwise rise and growth of the Tibet plateau. Science 294, 1671-1677.
Tarling, D., Hrouda, F., 1993. Magnetic anisotropy of rocks. Springer Science & Business Media.
Tian, X., Bai, Z., Klemperer, S.L., Liang, X., Liu, Z., Wang, X., Yang, X., Wei, Y., Zhu, G., 2021. Crustal-scale wedge tectonics at the narrow boundary between the Tibetan Plateau and Ordos block. Earth Planetary Science Letters 554, 116700.
Tian, X., Zhang, Z., 2013. Bulk crustal properties in NE Tibet and their implications for deformation model. Gondwana Research 24, 548-559.
Wang, C., Gao, R., Yin, A., Wang, H., Zhang, Y., Guo, T., Li, Q., Li, Y., 2011. A mid-crustal strain-transfer model for continental deformation: A new perspective from high-resolution deep seismic-reflection profiling across NE Tibet. Earth Planetary Science Letters 306, 279-288.
Wang, H., Gao, R., Yin, A., Xiong, X., Kuang, C., Li, W., Huang, W., 2012. Deep structure geometry features of Haiyuan Fault and deformation of the crust revealed by deep seismic reflection profiling. Chinese Journal of Geophysics 55, 3902-3909.
Wang, W., Zhang, P., Pang, J., Garzione, C., Zhang, H., Liu, C., Zheng, D., Zheng, W., Yu, J., 2016. The Cenozoic growth of the Qilian Shan in the northeastern Tibetan Plateau: A sedimentary archive from the Jiuxi Basin. Journal of Geophysical Research: Solid Earth 121, 2235-2257.
Wang, W., Zheng, W., Zhang, P., Li, Q., Kirby, E., Yuan, D., Zheng, D., Liu, C., Wang, Z., Zhang, H., 2017.

Expansion of the Tibetan Plateau during the Neogene. Nature communications 8, 15887.

Weil, A.B., Yonkee, W.A., 2012. Layer-parallel shortening across the Sevier fold-thrust belt and Laramide foreland of Wyoming: spatial and temporal evolution of a complex geodynamic system. Earth Planetary Science Letters 357, 405-420.

Wolf, G.S., Huismans, S.R., Braun, J., Yuan, X., 2022. Topography of mountain belts controlled by rheology and surface processes. Nature, 1-6.

Wu, J., Guo, L., Xiong, S., Wang, S., Tang, Z., Jin, C., Yang, X., Gu, N., Li, C., Cui, J., 2019. New Magnetic Constraints on Early-Middle Miocene Uplift of the Liupan Shan, Northeastern Margin of the Tibetan Plateau. Geochemistry, Geophysics, Geosystems 20, 1340-1357.

Wu, L., Xiao, A., Wang, L., Shen, Z., Zhou, S., Chen, Y., Wang, L., Liu, D., Guan, J., 2011. Late Jurassic–Early Cretaceous Northern Qaidam Basin, NW China: Implications for the earliest Cretaceous intracontinental tectonism. Cretaceous Research 32, 552-564.

Wu, L., Xiao, A., Yang, S., Wang, L., Mao, L., Wang, L., Dong, Y., Xu, B., 2012. Two-stage evolution of the Altyn Tagh Fault during the Cenozoic: new insight from provenance analysis of a geological section in NW Qaidam Basin, NW China. Terra Nova 24, 387-395.

Xiao, Q., Shao, G., Liu-Zeng, J., Oskin, M.E., Zhang, J., Zhao, G., Wang, J., 2015. Eastern termination of the Altyn Tagh Fault, western China: Constraints from a magnetotelluric survey. Journal of Geophysical Research: Solid Earth 120, 2838-2858.

Yan, M., VanderVoo, R., Fang, X., Parés, J.M., Rea, D.K., 2006. Paleomagnetic evidence for a mid-Miocene clockwise rotation of about 25 of the Guide Basin area in NE Tibet. Earth Planetary Science Letters 241, 234-247.

Ye, Z., Gao, R., Li, Q., Zhang, H., Shen, X., Liu, X., Gong, C., 2015. Seismic evidence for the North China plate underthrusting beneath northeastern Tibet and its implications for plateau growth. Earth Planetary Science Letters 426, 109-117.

Ye, Z., Gao, R., Lu, Z., Yang, Z., Xiong, X., Li, W., Huang, X., Liang, H., Qi, R., Shi, Z., 2021. A lithospheric-scale thrust-wedge model for the formation of the northern Tibetan plateau margin: Evidence from high-resolution seismic imaging. Earth Planetary Science Letters 574, 117170.

Yin, A., Dang, Y., Wang, L., Jiang, W., Zhou, S., Chen, X., Gehrels, G., McRivette, M., 2008. Cenozoic tectonic evolution of Qaidam basin and its surrounding regions (Part 1): The southern Qilian Shan-Nan Shan thrust belt and northern Qaidam basin. Geological Society of America Bulletin 120, 813-846.

Yin, A., Harrison, T.M., 2000. Geologic evolution of the Himalayan-Tibetan orogen. Annual Review of Earth Planetary Sciences 28, 211-280.

Yin, A., Rumelhart, P., Butler, R., Cowgill, E., Harrison, T., Foster, D., Ingersoll, R., Qing, Z., Xian-Qiang, Z., Xiao-Feng, W., 2002. Tectonic history of the Altyn Tagh fault system in northern Tibet inferred from Cenozoic sedimentation. Geological Society of America Bulletin 114, 1257.

Yu, J., Pang, J., Wang, Y., Zheng, D., Liu, C., Wang, W., Li, Y., Li, C., Xiao, L., 2019. Mid-Miocene uplift of the northern Qilian Shan as a result of the northward growth of the northern Tibetan Plateau. Geosphere 15, 423-432.

Yu, X., Huang, B., Guan, S., Fu, S., Cheng, F., Cheng, X., Zhang, T., Guo, Z., 2014a. Anisotropy of magnetic susceptibility of Eocene and Miocene sediments in the Qaidam Basin, Northwest China: Implication for Cenozoic tectonic transition and depocenter migration. Geochemistry, Geophysics, Geosystems 15, 2095-2108.

Yu, X., Fu, S., Guan, S., Huang, B., Cheng, F., Cheng, X., Zhang, T., Guo, Z., 2014b. Paleomagnetism of Eocene and Miocene sediments from the Qaidam basin: implication for no integral rotation since the Eocene and a rigid Qaidam block. Geochemistry, Geophysics, Geosystems 15, 2109-2127.

978 Yuan, D., Ge, W., Chen, Z., Li, C., Wang, Z., Zhang, H., 2013. The growth of northeastern Tibet and its relevance
979 to large-scale continental geodynamics: A review of recent studies. Tectonics 32(5), 1358-1370.
980 Yue, Y., Liou, J.G., 1999. Two-stage evolution model for the Altyn Tagh fault, China. Geology 27, 227-230.
981 Zhang, J., Cunningham, D., Qu, J., Zhang, B., Li, J., Zhao, H., Niu, P., Hui, J., Yun, L., Zhao, S., 2022. Poly-phase
982 structural evolution of the northeastern Alxa Block, China: Constraining the Paleozoic-Recent history of the
983 southern central Asian Orogenic belt. Gondwana Research 105, 25-50.
984 Zhang, P., Shen, Z., Wang, M., Gan, W., Burgmann, R., Molnar, P., 2004. Continuous deformation of the Tibetan
985 Plateau from global positioning system data. Geology 32(9), 809-812.
986 Zhang, P.Z., Molnar, P., Xu, X., 2007. Late Quaternary and present-day rates of slip along the Altyn Tagh Fault,
987 northern margin of the Tibetan Plateau. Tectonics 26, TC5010.
988 Zhang, Y.Q., Vergely, P., Mercier, J., 1995. Active faulting in and along the Qinling Range (China) inferred from
989 SPOT imagery analysis and extrusion tectonics of south China. Tectonophysics 243, 69-95.
990 Zhao, J., Jin, Z., Mooney, W.D., Okaya, N., Wang, S., Gao, X., Tang, L., Pei, S., Liu, H., Xu, Q., 2013. Crustal
991 structure of the central Qaidam basin imaged by seismic wide-angle reflection/refraction profiling.
992 Tectonophysics 584, 174-190.
993 Zheng, D., Zhang, P., Wan, J., Yuan, D., Li, C., Yin, G., Zhang, G., Wang, Z., Min, W., Chen, J., 2006. Rapid
994 exhumation at~ 8 Ma on the Liupan Shan thrust fault from apatite fission-track thermochronology: Implications
995 for growth of the northeastern Tibetan Plateau margin. Earth Planetary Science Letters 248, 198-208.
996 Zheng, D., Zhang, P., Wan, J., Li, C., Cao, J., 2003. Late Cenozoic deformation subsequence in northeastern
997 margin of Tibet—Detrital AFT records from Linxia Basin. Science in China Series D: Earth Sciences 46,
998 266-275.
999 Zheng, H., Wei, X., Tada, R., Clift, P.D., Wang, B., Jourdan, F., Wang, P., He, M., 2015. Late oligocene–early
1000 miocene birth of the Taklimakan Desert. Proceedings of the National Academy of Sciences 112, 7662-7667.
1001 Zheng, W., Zhang, P., He, W., Yuan, D., Shao, Y., Zheng, D., Ge, W., Min, W., 2013. Transformation of
1002 displacement between strike-slip and crustal shortening in the northern margin of the Tibetan Plateau: Evidence
1003 from decadal GPS measurements and late Quaternary slip rates on faults. Tectonophysics 584, 267-280.
1004 Zhu, L., Helmberger, D.V., 1998. Moho offset across the northern margin of the Tibetan Plateau. Science 281,
1005 1170-1172.
1006 Zhuang, G., Hourigan, J.K., Ritts, B.D., Kent-Corson, M.L., 2011. Cenozoic multiple-phase tectonic evolution of
1007 the northern Tibetan Plateau: Constraints from sedimentary records from Qaidam basin, Hexi Corridor, and
1008 Subei basin, northwest China. American Journal of Science 311, 116-152.
1009 Zhuang, G., Johnstone, S.A., Hourigan, J., Ritts, B., Robinson, A., Sobel, E.R., 2018. Understanding the geologic
1010 evolution of Northern Tibetan Plateau with multiple thermochronometers. Gondwana Research 58, 195-210.
1011 Zuza, A.V., Yin, A., 2016. Continental deformation accommodated by non-rigid passive bookshelf faulting: An
1012 example from the Cenozoic tectonic development of northern Tibet. Tectonophysics 677, 227-240.

Figure1.

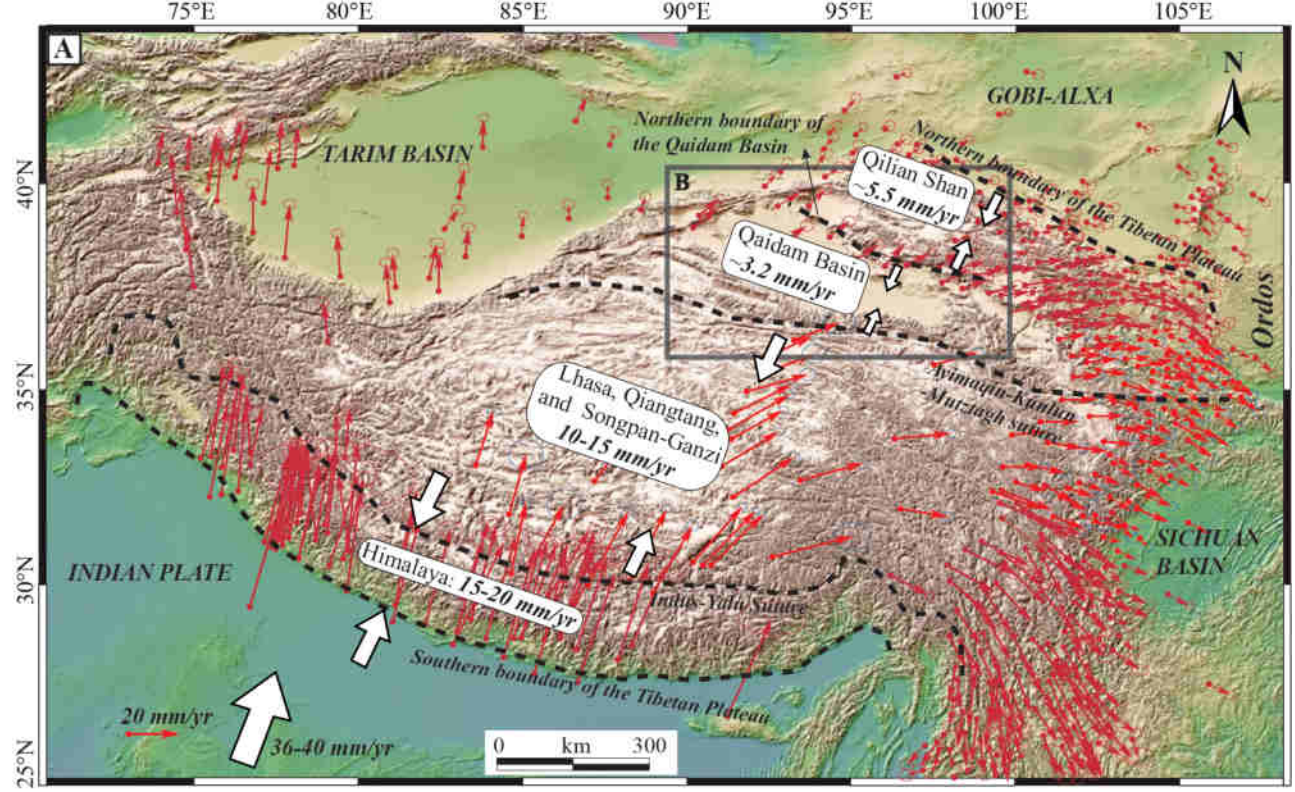

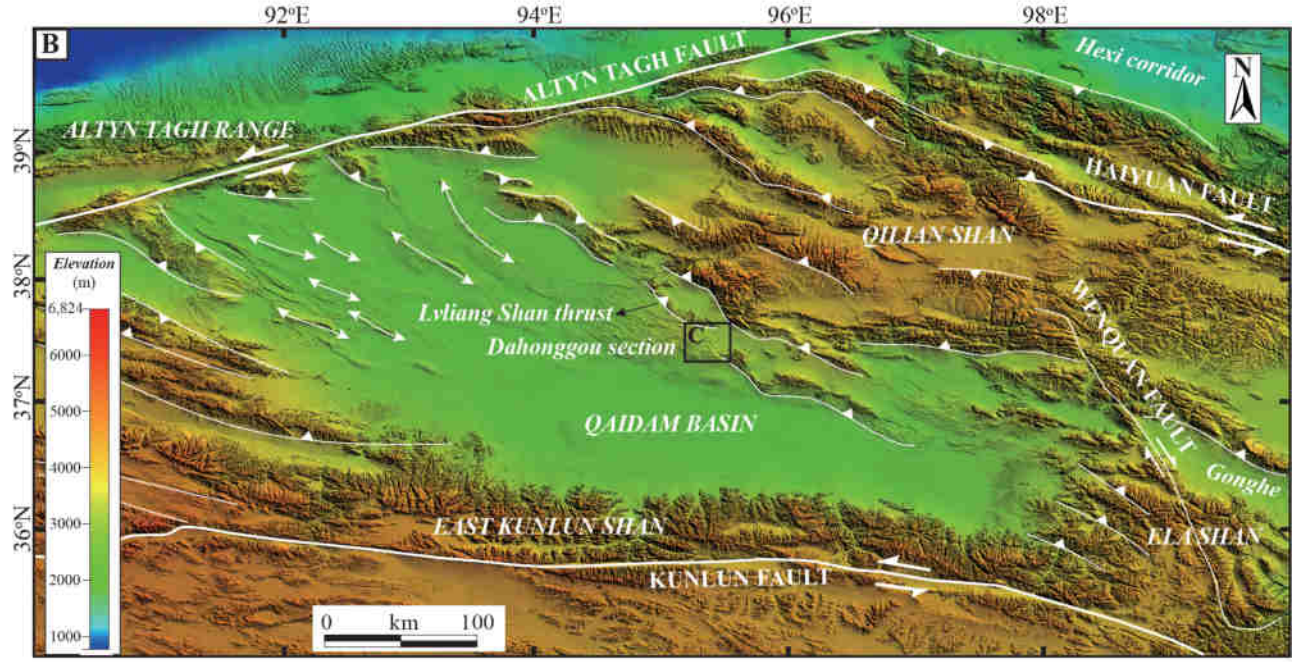

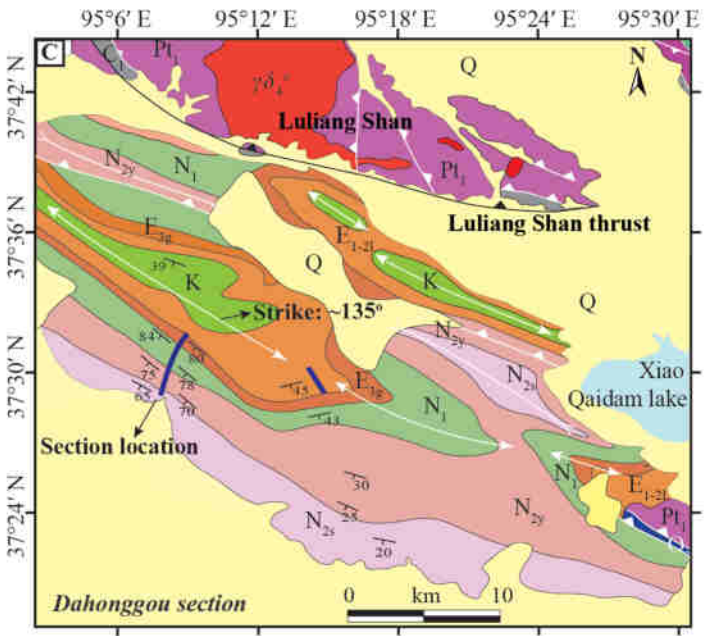

Q Qigequan Fm.
N_{2s} Shizigou Fm.
N_{2y} Upper Youshashan Fm.
N_1 Lower Youshashan Fm.
Upper Ganchaigou Fm.
E_{3g} Lower Ganchaigou Fm.
E_{1-2l} Lulehe Fm.
K Cretaceous Quanyagou Fm.
C_1 Carboniferous metamorphic rocks
O_1 Ordovician metamorphic rocks
Pt_1 Proterozoic metamorphic rocks
$\gamma\delta_4^3$ Permian granitoids
Thrust fault
Strike-slip fault
Anticline
Syncline
45 Bedding attitude
Studied section

Figure2.

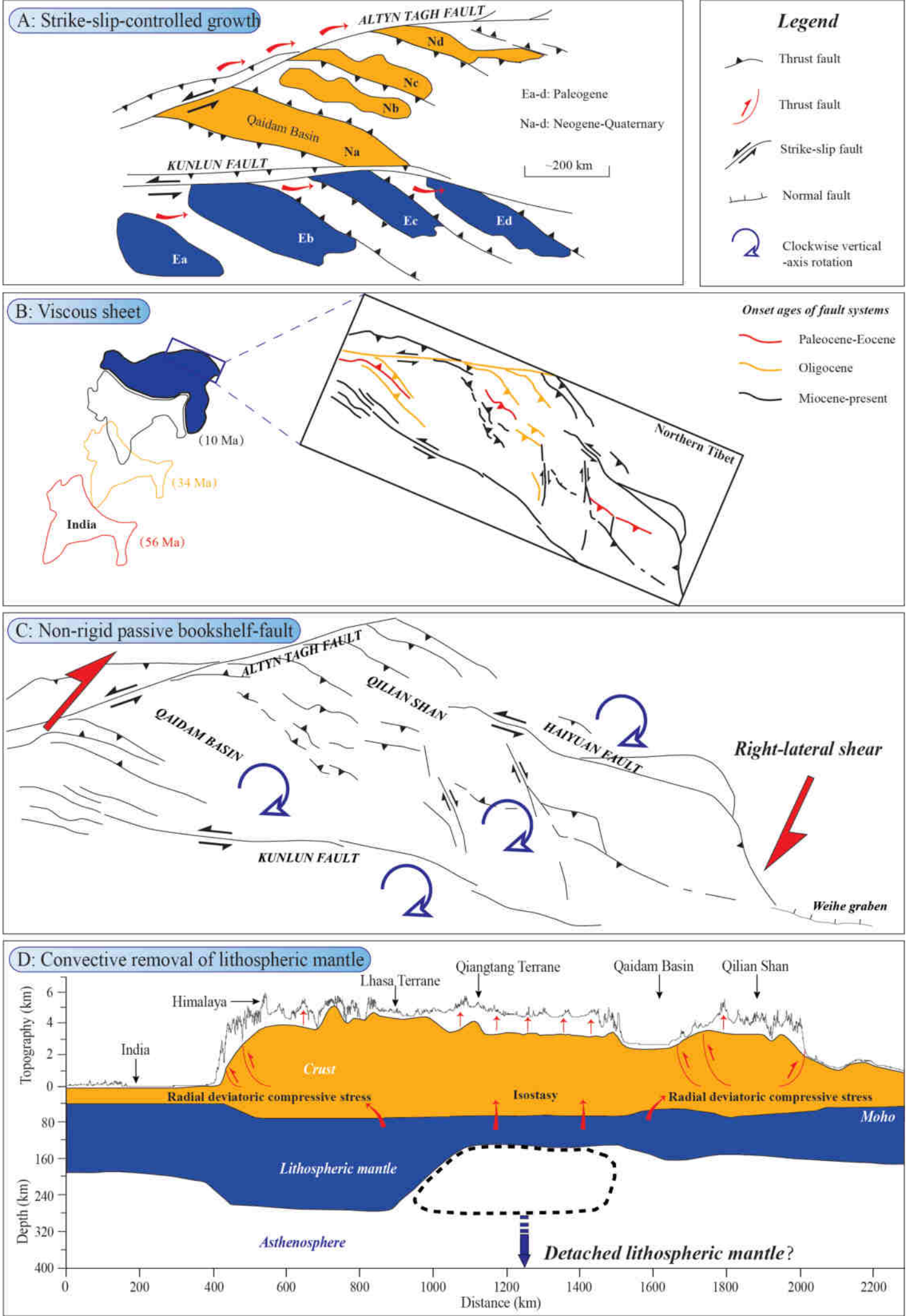
A: Strike-slip-controlled growth
ALTYN TAGH FAULT
Nd
Nc
Nb
Qaidam Basin
Na
KUNLUN FAULT
Ea
Eb
Ec
Ed
Ea-d: Paleogene
Na-d: Neogene-Quaternary
~200 km
Legend
Thrust fault
Thrust fault
Strike-slip fault
Normal fault
Clockwise vertical -axis rotation
B: Viscous sheet
(10 Ma)
(34 Ma)
India
(56 Ma)
Northern Tibet
Onset ages of fault systems
Paleocene-Eocene
Oligocene
Miocene-present
C: Non-rigid passive bookshelf-fault
ALTYN TAGH FAULT
QILIAN SHAN
QAIDAM BASIN
HAIYUAN FAULT
KUNLUN FAULT
Right-lateral shear
Weihe graben
D: Convective removal of lithospheric mantle
Himalaya
Lhasa Terrane
Qiangtang Terrane
Qaidam Basin
Qilian Shan
India
Crust
Radial deviatoric compressive stress
Isostasy
Radial deviatoric compressive stress
Moho
Lithospheric mantle
Asthenosphere
Detached lithospheric mantle?
Topography (km)
Depth (km)
Distance (km)
6
4
2
0
80
160
240
320
400
0
200
400
600
800
1000
1200
1400
1600
1800
2000
2200

Figure3.

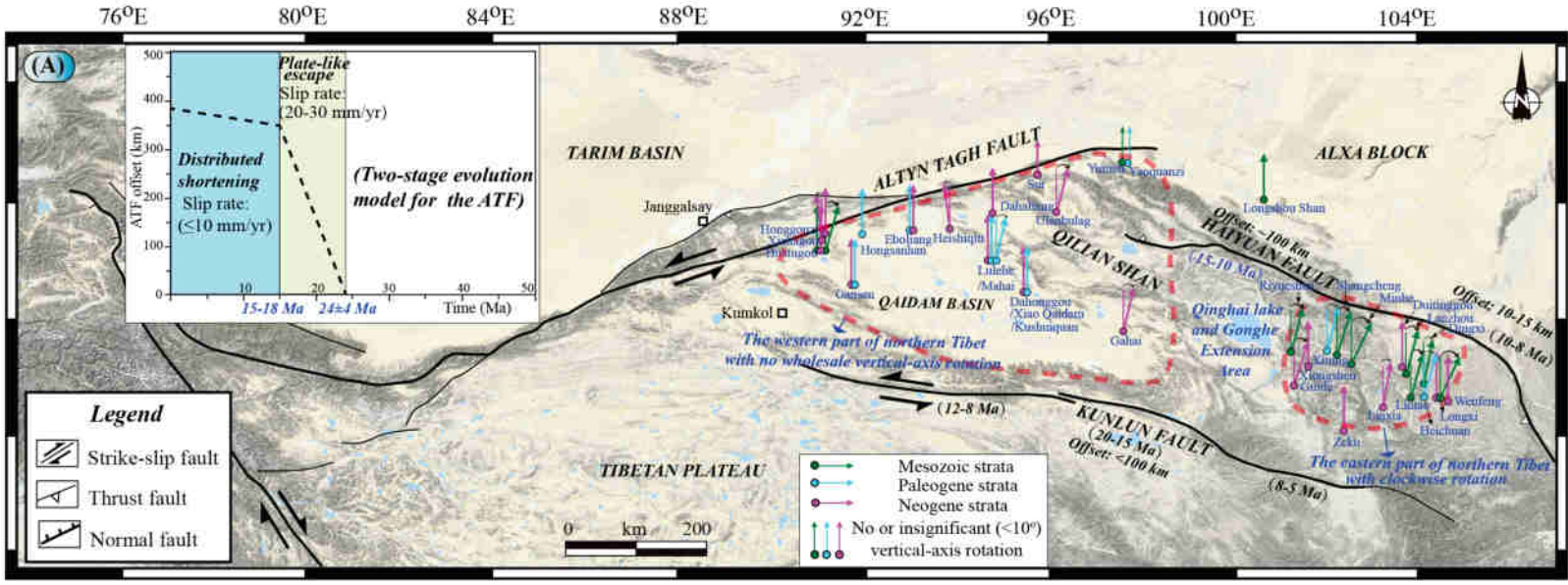
(A)
ATF offset (km)
Plate-like escape
Slip rate:
(20-30 mm/yr)
Distributed shortening
Slip rate:
(≤10 mm/yr)
(Two-stage evolution model for the ATF)
15-18 Ma
24±4 Ma
Time (Ma)
TARIM BASIN
ALTYN TAGH FAULT
ALXA BLOCK
Janggalsay
Kumkol
QAIDAM BASIN
QILIAN SHAN
HAIYUAN FAULT
(15-10 Ma)
Offset: ~100 km
Offset: 10-15 km
(10-8 Ma)
Qinghai lake and Gonghe Extension Area
The western part of northern Tibet with no wholesale vertical-axis rotation
(12-8 Ma)
KUNLUN FAULT
(20-15 Ma)
Offset: <100 km
(8-5 Ma)
The eastern part of northern Tibet with clockwise rotation
TIBETAN PLATEAU
0 km 200
Legend
Strike-slip fault
Thrust fault
Normal fault
Mesozoic strata
Paleogene strata
Neogene strata
No or insignificant (<10°) vertical-axis rotation
76°E
80°E
84°E
88°E
92°E
96°E
100°E
104°E
39°N
35°N

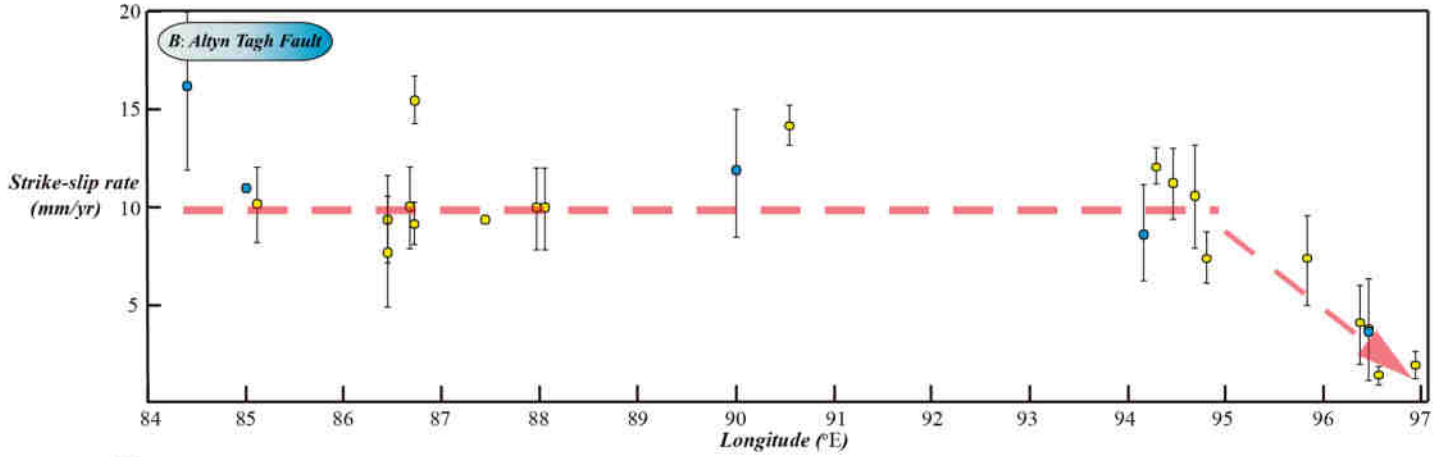
B: Altyn Tagh Fault
Strike-slip rate (mm/yr)
Longitude (°E)

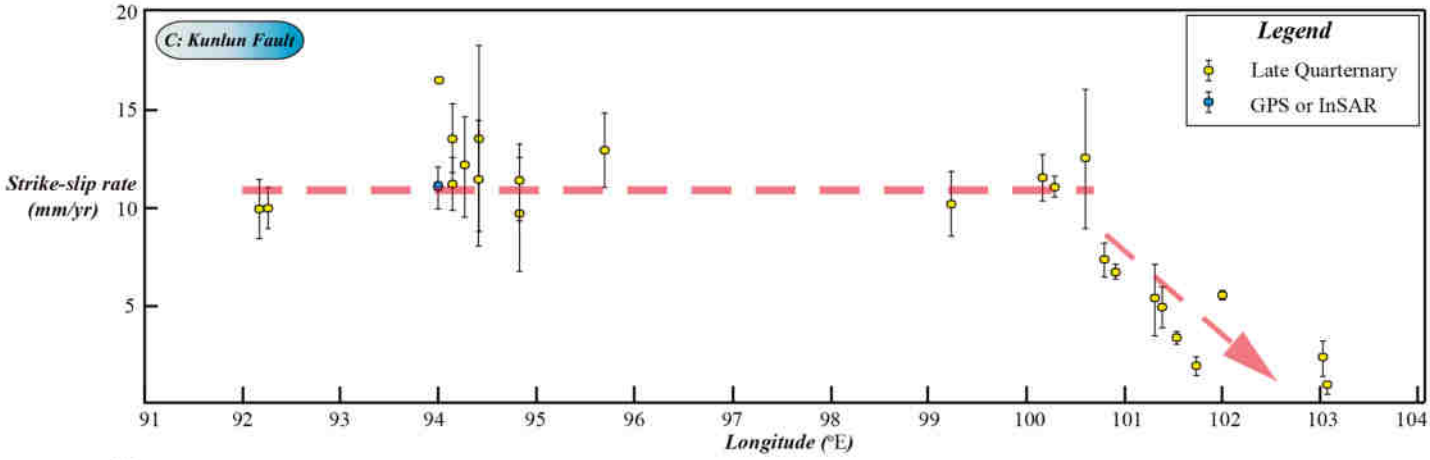
C: Kunlun Fault
Legend
Late Quarternary
GPS or InSAR
Strike-slip rate (mm/yr)
Longitude (°E)

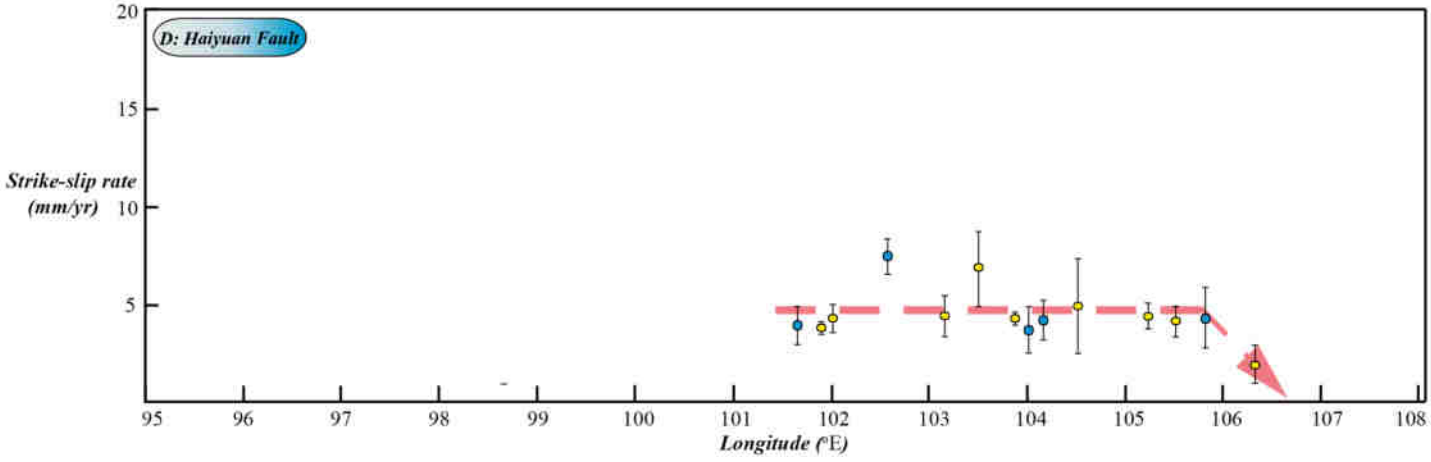
D: Haiyuan Fault
Strike-slip rate (mm/yr)
Longitude (°E)

Figure4.

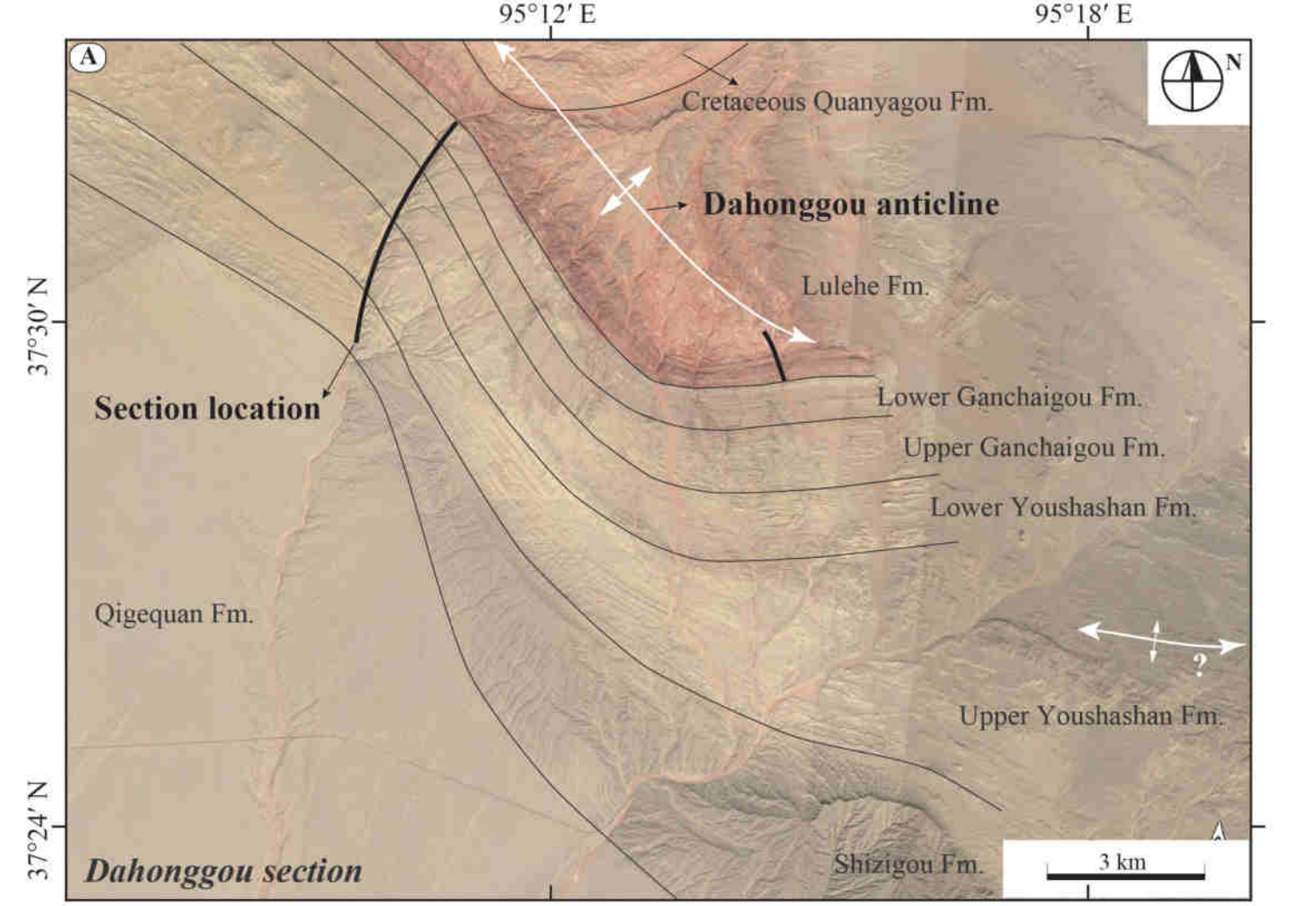
95°12′ E
95°18′ E
37°30′ N
37°24′ N
A
N
Cretaceous Quanyagou Fm.
Dahonggou anticline
Lulehe Fm.
Section location
Lower Ganchaigou Fm.
Upper Ganchaigou Fm.
Lower Youshashan Fm.
Qigequan Fm.
?
Upper Youshashan Fm.
Dahonggou section
Shizigou Fm.
3 km


C
NW
2 m
Lulehe Fm.
conglomerate+sandstone


D
SE
Lulehe Fm.
Lower Ganchaigou Fm.
mudstone+siltstone


E
SW
Upper Ganchaigou Fm.
mudstone+siltstone

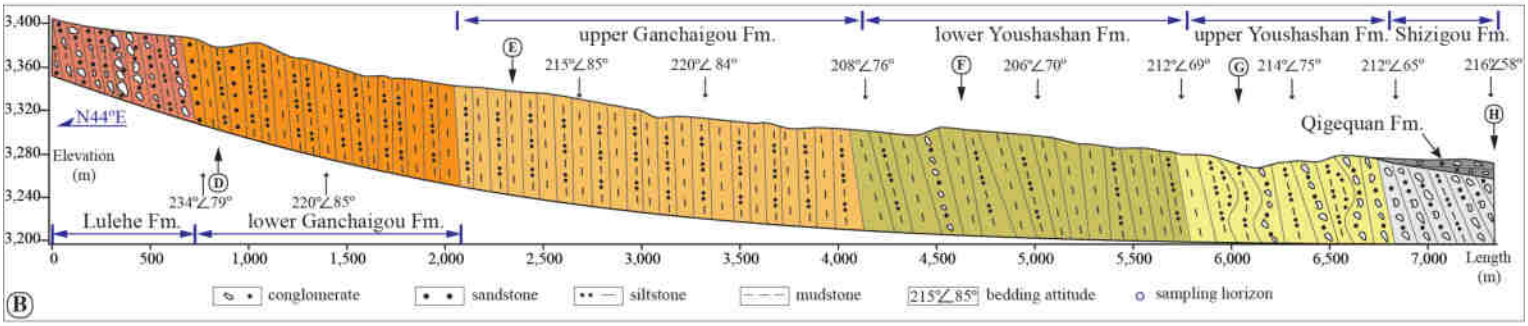
upper Ganchaigou Fm.
lower Youshashan Fm.
upper Youshashan Fm.
Shizigou Fm.
E
F
G
H
215°∠85°
220°∠84°
208°∠76°
206°∠70°
212°∠69°
214°∠75°
212°∠65°
216°∠58°
N44°E
Elevation (m)
3,400
3,360
3,320
3,280
3,240
3,200
D
234°∠79°
220°∠85°
Lulehe Fm.
lower Ganchaigou Fm.
Qigequan Fm.
0
500
1,000
1,500
2,000
2,500
3,000
3,500
4,000
4,500
5,000
5,500
6,000
6,500
7,000
Length (m)
B
conglomerate
sandstone
siltstone
mudstone
215°∠85° bedding attitude
sampling horizon


F
SW
Lower Youshashan Fm.
mudstone+siltstone


G
NE
1 m
Upper Youshashan Fm.
conglomerate+sandstone

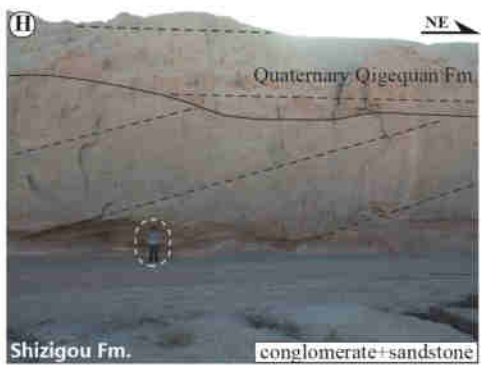
H
NE
Quaternary Qigequan Fm.
Shizigou Fm.
conglomerate+sandstone

Figure5.

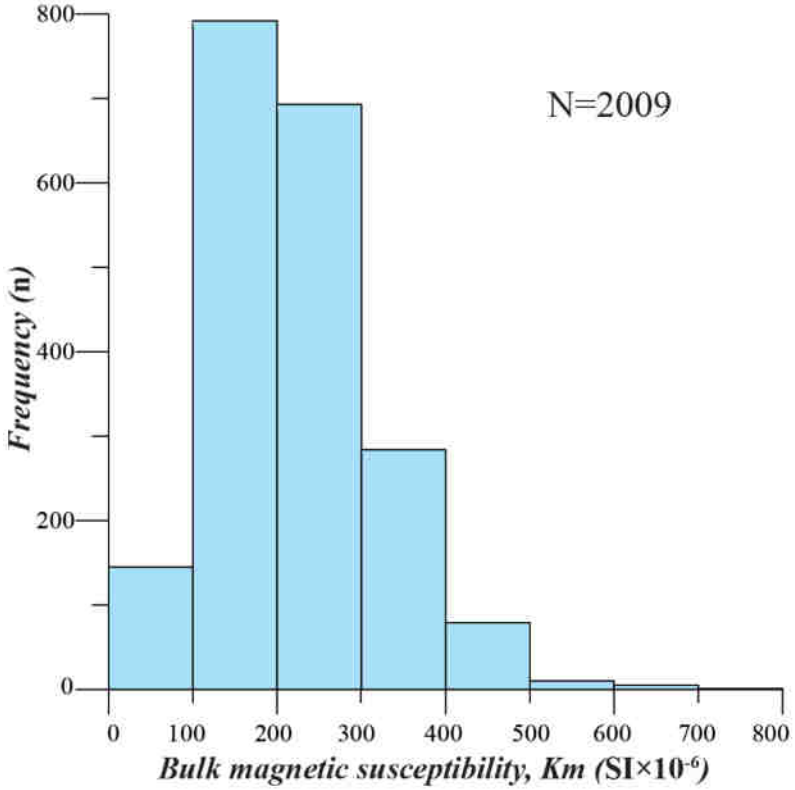
N=2009
Frequency (n)
Bulk magnetic susceptibility, Km (SI×10⁻⁶)

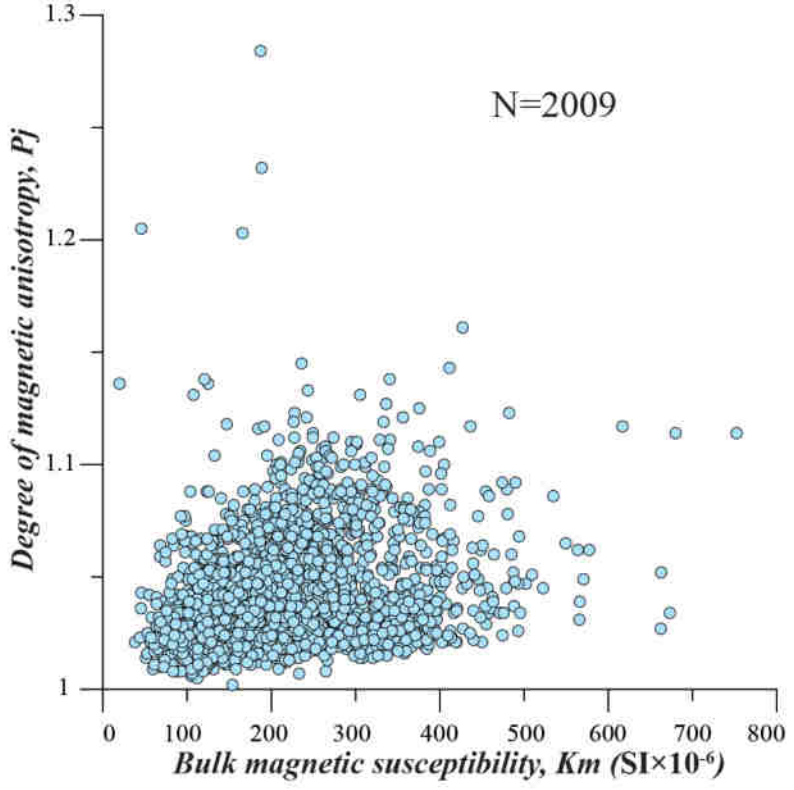
N=2009
Degree of magnetic anisotropy, Pj
Bulk magnetic susceptibility, Km (SI×10⁻⁶)

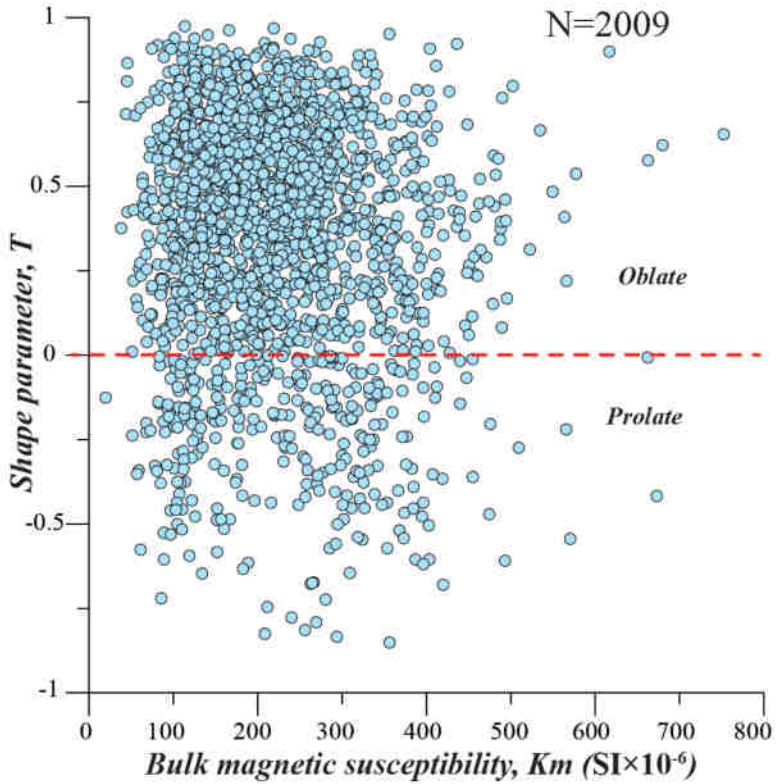
N=2009
Shape parameter, T
Oblate
Prolate
Bulk magnetic susceptibility, Km (SI×10⁻⁶)

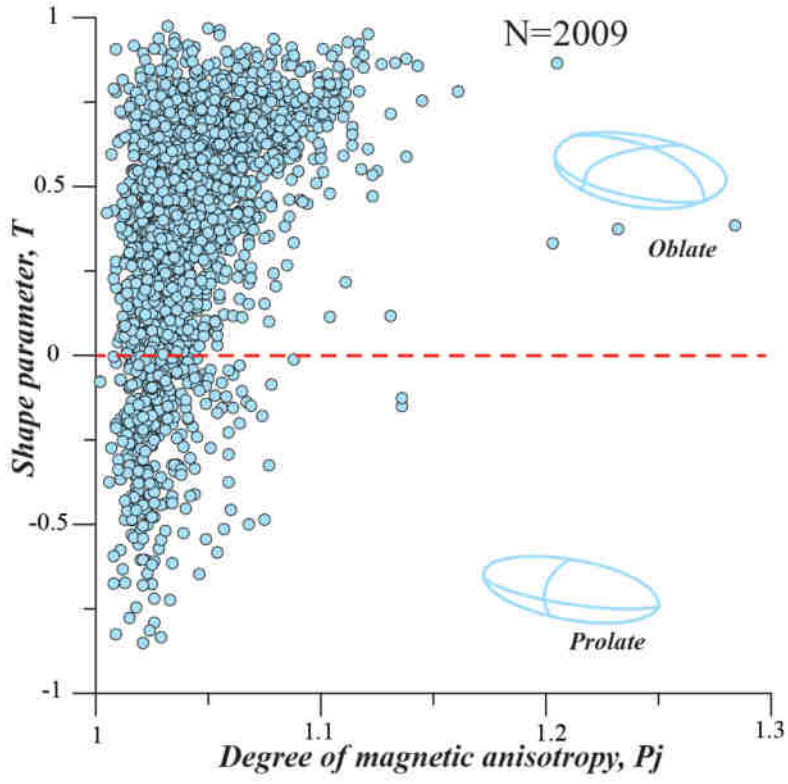
N=2009
Shape parameter, T
Oblate
Prolate
Degree of magnetic anisotropy, Pj

Figure6.

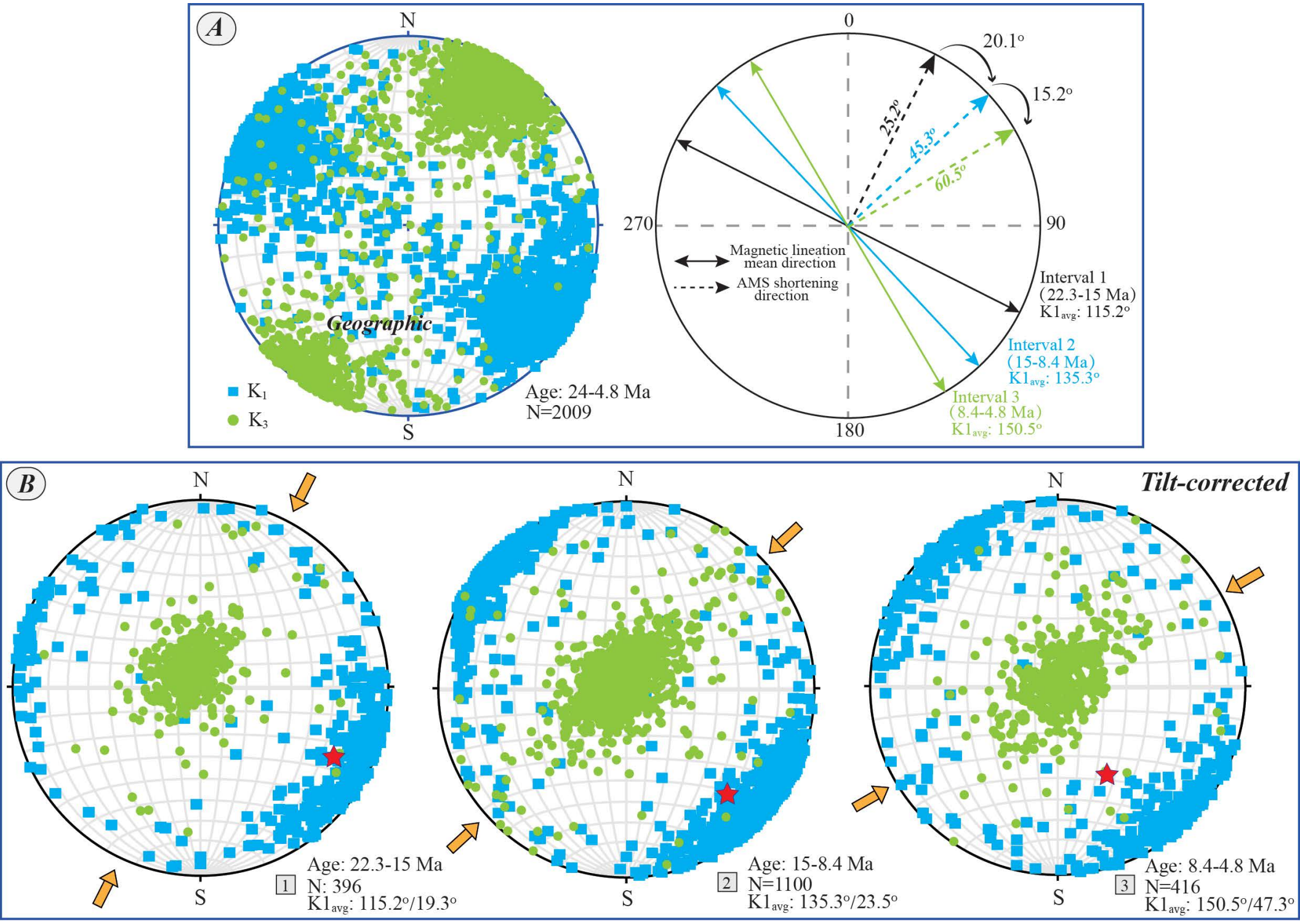
A
N
S
Geographic
K1
K3
Age: 24-4.8 Ma
N=2009
0
90
180
270
20.1°
15.2°
25.2°
45.3°
60.5°
Magnetic lineation mean direction
AMS shortening direction
Interval 1 (22.3-15 Ma) K1avg: 115.2°
Interval 2 (15-8.4 Ma) K1avg: 135.3°
Interval 3 (8.4-4.8 Ma) K1avg: 150.5°
B
Tilt-corrected
1 Age: 22.3-15 Ma N: 396 K1avg: 115.2°/19.3°
2 Age: 15-8.4 Ma N=1100 K1avg: 135.3°/23.5°
3 Age: 8.4-4.8 Ma N=416 K1avg: 150.5°/47.3°

Figure7.

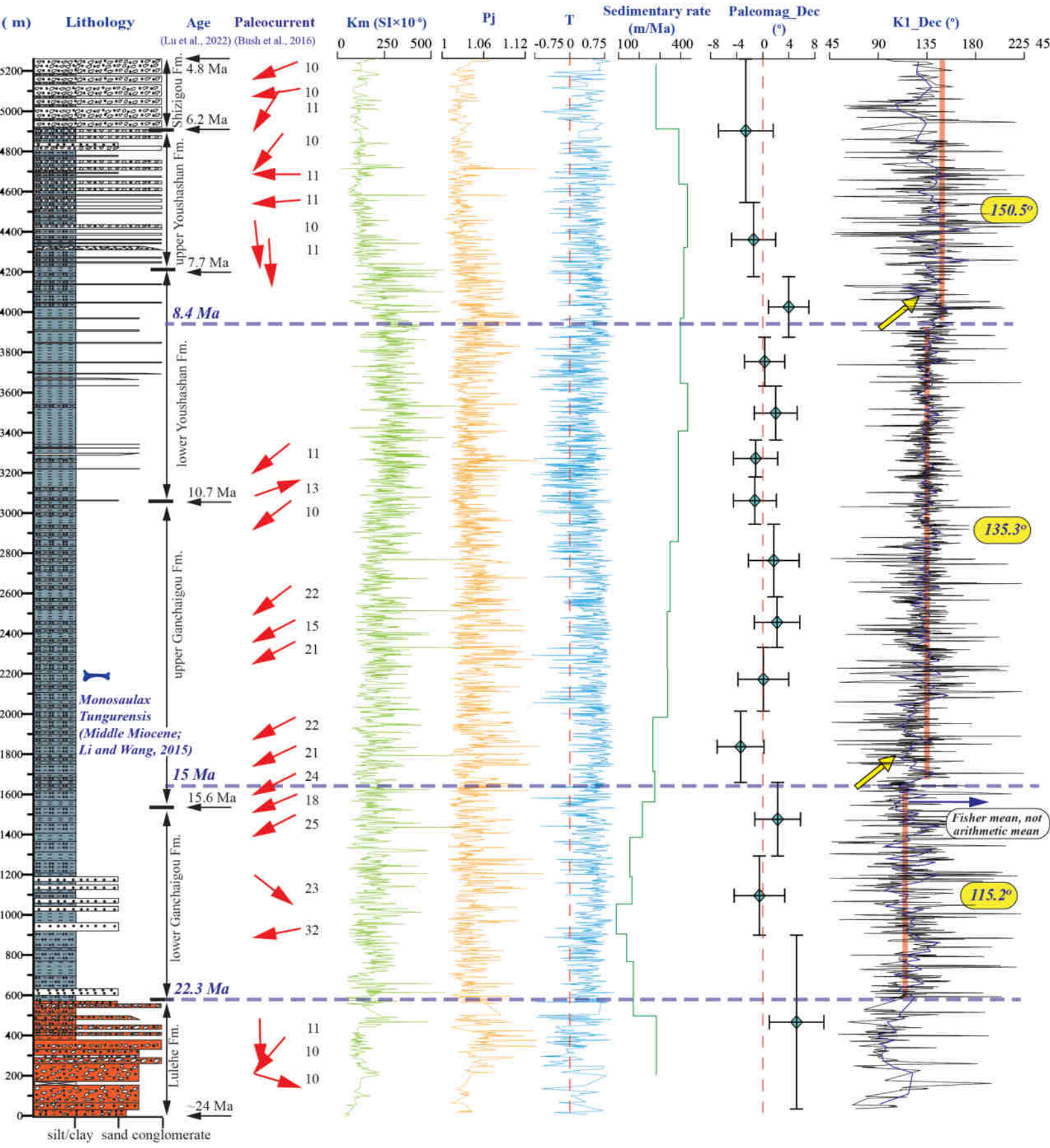
(m)
Lithology
Age
(Lu et al., 2022)
Paleocurrent
(Bush et al., 2016)
Km (SI×10⁻⁶)
Pj
T
Sedimentary rate (m/Ma)
Paleomag_Dec (°)
K1_Dec (°)
Shizigou Fm.
upper Youshashan Fm.
lower Youshashan Fm.
upper Ganchaigou Fm.
lower Ganchaigou Fm.
Lulehe Fm.
4.8 Ma
6.2 Ma
7.7 Ma
8.4 Ma
10.7 Ma
15 Ma
15.6 Ma
22.3 Ma
~24 Ma
Monosaulax Tungurensis (Middle Miocene; Li and Wang, 2015)
150.5°
135.3°
115.2°
Fisher mean, not arithmetic mean
silt/clay
sand
conglomerate

Figure8.

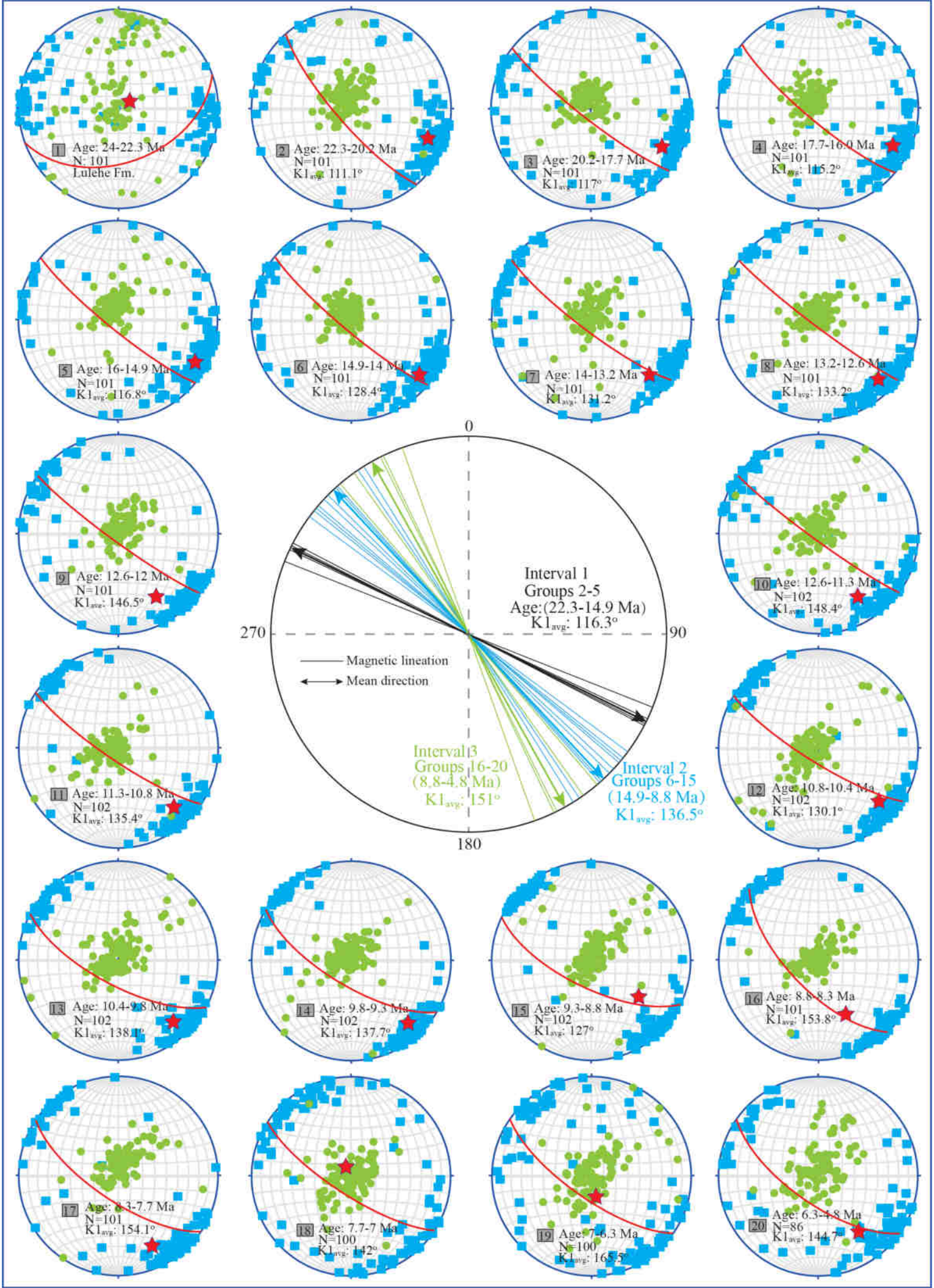
1 Age: 24-22.3 Ma
N: 101
Lulehe Fm.
2 Age: 22.3-20.2 Ma
N=101
K1avg: 111.1°
3 Age: 20.2-17.7 Ma
N=101
K1avg: 117°
4 Age: 17.7-16.0 Ma
N=101
K1avg: 115.2°
5 Age: 16-14.9 Ma
N=101
K1avg: 116.8°
6 Age: 14.9-14 Ma
N=101
K1avg: 128.4°
7 Age: 14-13.2 Ma
N=101
K1avg: 131.2°
8 Age: 13.2-12.6 Ma
N=101
K1avg: 133.2°
9 Age: 12.6-12 Ma
N=101
K1avg: 146.5°
10 Age: 12.6-11.3 Ma
N=102
K1avg: 148.4°
11 Age: 11.3-10.8 Ma
N=102
K1avg: 135.4°
12 Age: 10.8-10.4 Ma
N=102
K1avg: 130.1°
13 Age: 10.4-9.8 Ma
N=102
K1avg: 138.1°
14 Age: 9.8-9.3 Ma
N=102
K1avg: 137.7°
15 Age: 9.3-8.8 Ma
N=102
K1avg: 127°
16 Age: 8.8-8.3 Ma
N=101
K1avg: 153.8°
17 Age: 8.3-7.7 Ma
N=101
K1avg: 154.1°
18 Age: 7.7-7 Ma
N=100
K1avg: 142°
19 Age: 7-6.3 Ma
N=100
K1avg: 165.5°
20 Age: 6.3-4.8 Ma
N=86
K1avg: 144.7°
0
90
180
270
Interval 1
Groups 2-5
Age:(22.3-14.9 Ma)
K1avg: 116.3°
Magnetic lineation
Mean direction
Interval 3
Groups 16-20
(8.8-4.8 Ma)
K1avg: 151°
Interval 2
Groups 6-15
(14.9-8.8 Ma)
K1avg: 136.5°

Figure9.

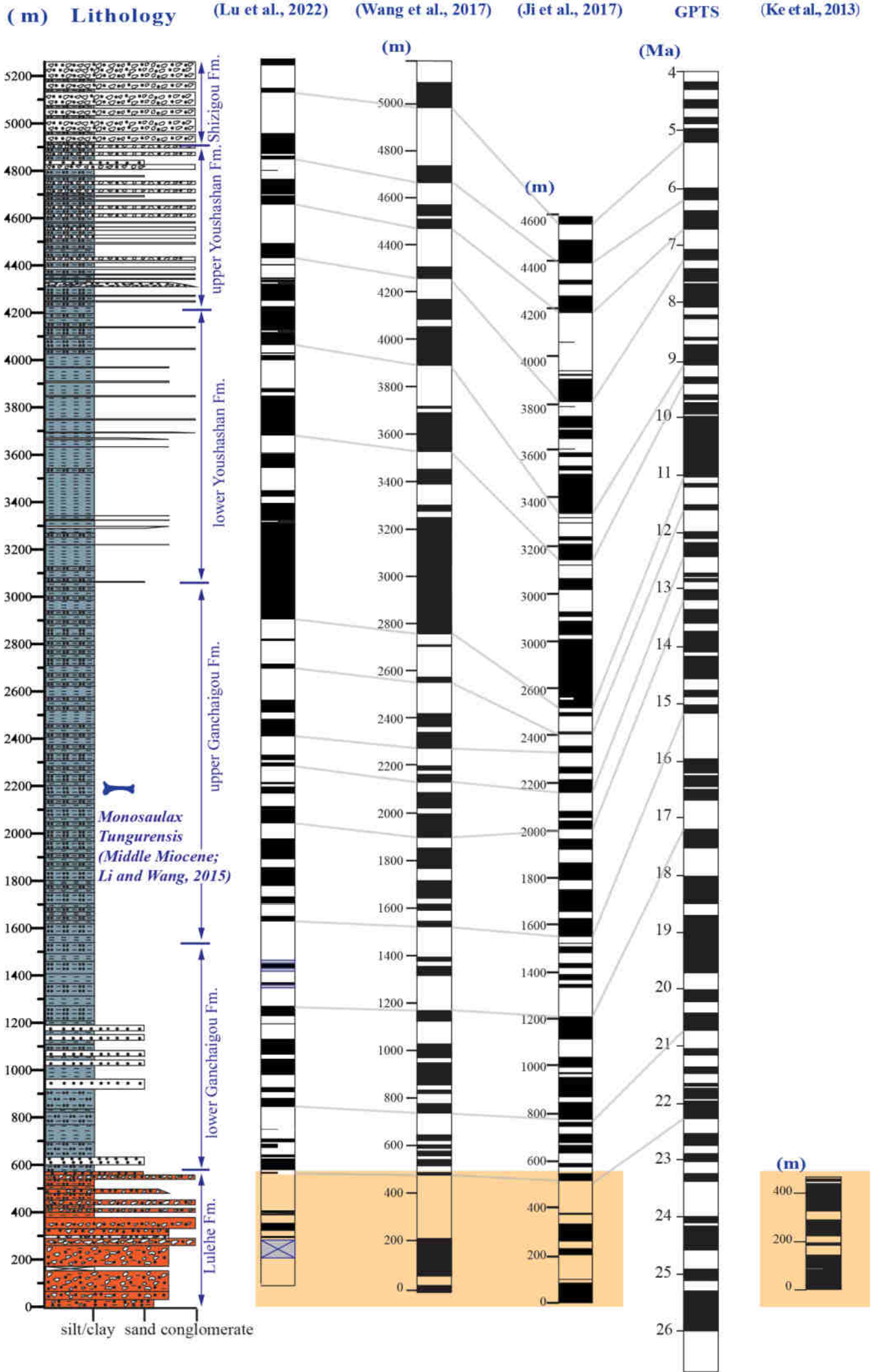
(m) Lithology
(Lu et al., 2022)
(Wang et al., 2017)
(Ji et al., 2017)
GPTS
(Ke et al., 2013)
(m)
(Ma)
upper Youshashan Fm.
Shizigou Fm.
lower Youshashan Fm.
upper Ganchaigou Fm.
lower Ganchaigou Fm.
Lulehe Fm.
Monosaulax Tungurensis (Middle Miocene; Li and Wang, 2015)
silt/clay
sand
conglomerate

Figure10.

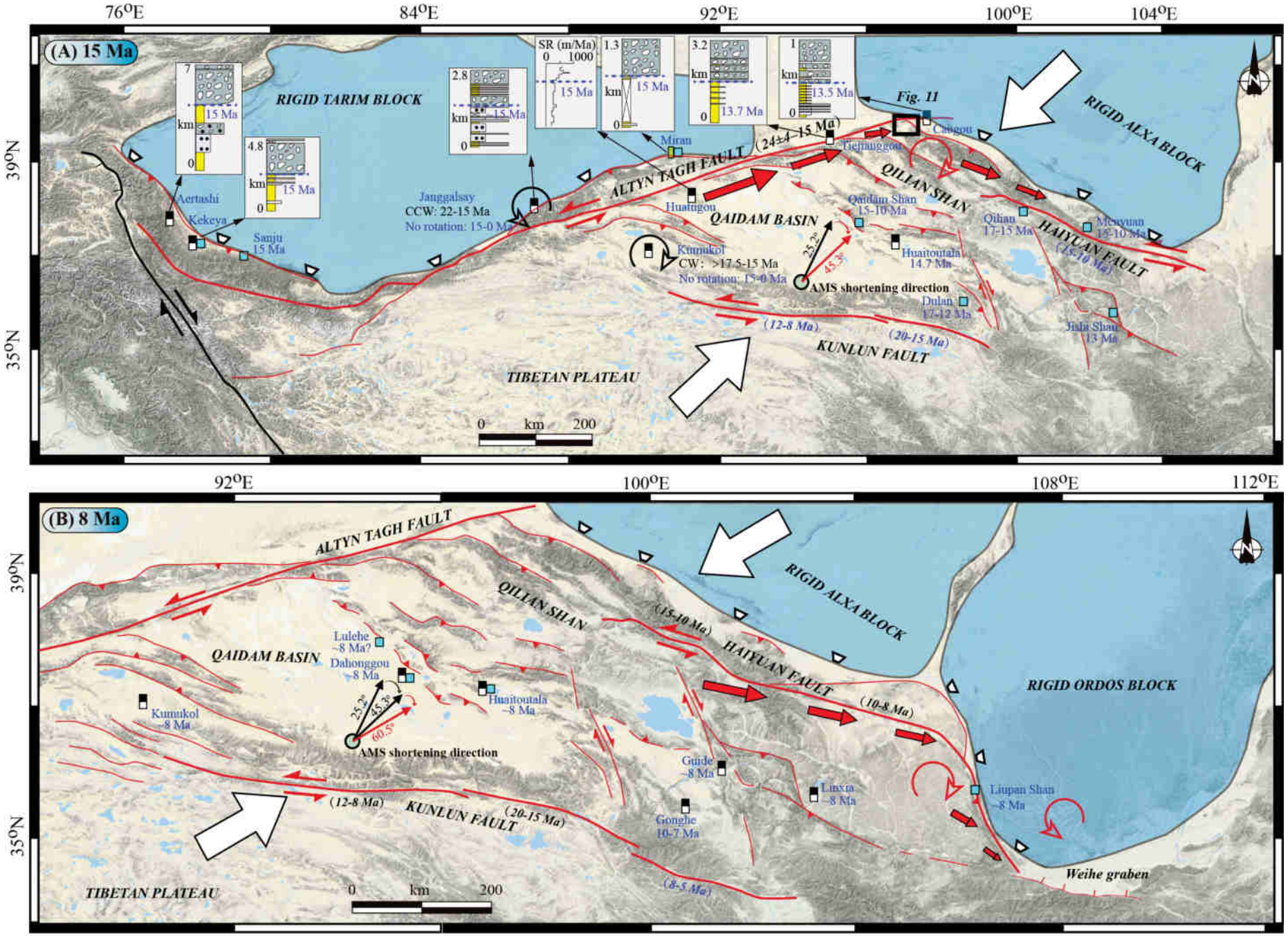
(A) 15 Ma
RIGID TARIM BLOCK
RIGID ALXA BLOCK
Fig. 11
ALTYN TAGH FAULT
(24±4-15 Ma)
QILIAN SHAN
QAIDAM BASIN
HAIYUAN FAULT
(15-10 Ma)
KUNLUN FAULT
(12-8 Ma)
(20-15 Ma)
TIBETAN PLATEAU
AMS shortening direction
Aertashi
Kekeya
Sanju
15 Ma
Jianggalsay
CCW: 22-15 Ma
No rotation: 15-0 Ma
Miran
Huatugou
Chagou
Dejinggou
Qaidam Shan
15-10 Ma
Qilian
17-15 Ma
Menyuan
15-10 Ma
Kumukol
CW: >17.5-15 Ma
No rotation: 15-0 Ma
Huaitoutala
14.7 Ma
Dulan
17-12 Ma
Jishi Shan
13 Ma
SR (m/Ma)
13.7 Ma
13.5 Ma
0 km 200
92°E
100°E
108°E
112°E
(B) 8 Ma
ALTYN TAGH FAULT
QILIAN SHAN
RIGID ALXA BLOCK
RIGID ORDOS BLOCK
QAIDAM BASIN
HAIYUAN FAULT
(15-10 Ma)
(10-8 Ma)
KUNLUN FAULT
(12-8 Ma)
(20-15 Ma)
(8-5 Ma)
TIBETAN PLATEAU
Weihe graben
AMS shortening direction
Lulehe
~8 Ma?
Dahonggou
~8 Ma
Huaitoutala
~8 Ma
Kumukol
~8 Ma
Guide
~8 Ma
Linxia
~8 Ma
Liupan Shan
~8 Ma
Gonghe
10-7 Ma
25.2°
45.3°
60.5°
0 km 200
39°N
35°N
Legend
Strike-slip fault
Thrust fault
Normal fault
Mudstone+siltstone
Conglomerate
Sandstone
Covered interval
Magnetostratigraphy
Low-temperature thermochronology
Clockwise (CW) vertical-axis rotation
Counterclockwise (CCW) vertical-axis rotation
CW rotation of paleostress field determined from AMS data
Shortening directions deduced from AMS data
Schematic resistence of rigid blocks
Schematic motion of crustal materials

Figure11.

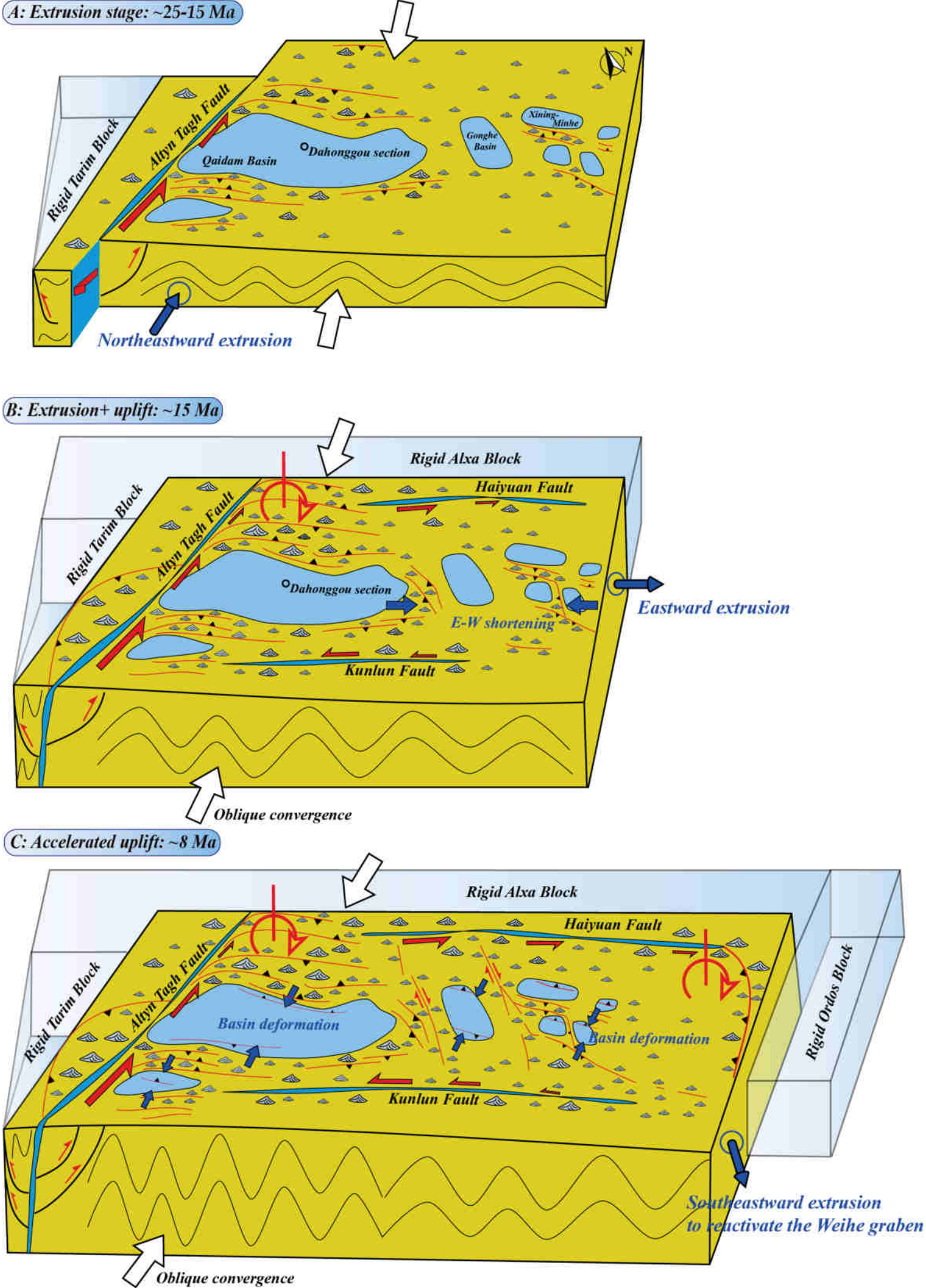
A: Extrusion stage: ~25-15 Ma
Rigid Tarim Block
Altyn Tagh Fault
Qaidam Basin
Dahonggou section
Gonghe Basin
Xining-Minhe
N
Northeastward extrusion
B: Extrusion+ uplift: ~15 Ma
Rigid Alxa Block
Haiyuan Fault
Rigid Tarim Block
Altyn Tagh Fault
Dahonggou section
E-W shortening
Eastward extrusion
Kunlun Fault
Oblique convergence
C: Accelerated uplift: ~8 Ma
Rigid Alxa Block
Haiyuan Fault
Rigid Tarim Block
Altyn Tagh Fault
Basin deformation
Basin deformation
Rigid Ordos Block
Kunlun Fault
Southeastward extrusion
to reactivate the Weihe graben
Oblique convergence